Optical Measurements in Non-Equilibrium Plasmas and Flows

W. Lempert
The Ohio State University, Columbus, OH
USA

1 Introduction

Thermal disequilibrium among the internal modes of molecular species in supersonic and hypersonic air flows, and in non-equilibrium air, and oxygen containing plasmas, is a widely occurring, but far from well understood, phenomenon which is important to a wide variety of aerodynamic and aerospace platforms. For example, energy storage in vibrational and low lying electronic states of the most common air species (N_2, O_2, NO), including the metastable states O_2 ($a^1\Delta_g$) and N_2 ($A\ ^3\sum_u^+$), are known to have significant, but incompletely understood, influences on the chemistry, shock structure, and heat transfer in the complex flow field around hypervelocity vehicles. The acceleration of low temperature oxidation kinetics by super-equilibrium concentrations of key radical species, such as O, H, OH, etc., produced in high pressure non-equilibrium discharges is similarly recognized but not well understood. In this lecture, an overview of laser diagnostic methods used to probe and characterize such environments will be presented, focusing on recent measurements in N_2, air, and other oxygen containing, nonequilibrium plasmas and high speed flows. The lecture will be divided into three parts. Section 2 will present an illustrative survey of laser diagnostic methods which have been successfully employed in measurements of rotational/translational temperature, vibrational distribution function, electronic meta-stable state concentrations, and positive ion and free electron number density. This survey, while by no means complete, is meant to provide the reader with an overview of the power of modern optical diagnostic methodologies and technologies, as well as to provide some guidance on the matching of diagnostic methods with measurement goals. In this section it is assumed that the reader has some familiarity with the spectroscopic fundamentals of atoms and diatomic molecules in the gas phase which serve as the foundation for each of the diagnostic measurements discussed, although some specific information relevant to the spectroscopic diagnostics of non-equilibrium systems will be provided. If necessary, more details on the spectroscopic fundamentals of modern laser diagnostics can be found in [1-5]. Section 3 will present a more detailed discussion of a recent study in which advanced laser diagnostics have been used in combination with modeling to study fundamental non-equilibrium low temperature Plasma Assisted Combustion kinetics. Section 4 will discuss recent advances in ultra-high frame rate imaging, which provides new capability for capturing the dynamic evolution of high speed, unsteady flow fields, and/or increasing the data collection rate in short run time "impulse" facilities.

2 Illustrative Survey of Laser Diagnostic Measurements in Non-Equilibrium Plasmas and Flows.

2.1 Rotational/Translational Temperature Measurements

Knowledge of the translational energy distribution, which in most cases will be in thermodynamic equilibrium with the rotational energy distribution, is a basic starting point for the characterization and study of non-equilibrium flows and plasmas. The determination of translational temperature is most often based on resolution of the absorption/fluorescence spectral

Report Documentation Page	*Form Approved* *OMB No. 0704-0188*

Public reporting burden for the collection of information is estimated to average 1 hour per response, including the time for reviewing instructions, searching existing data sources, gathering and maintaining the data needed, and completing and reviewing the collection of information. Send comments regarding this burden estimate or any other aspect of this collection of information, including suggestions for reducing this burden, to Washington Headquarters Services, Directorate for Information Operations and Reports, 1215 Jefferson Davis Highway, Suite 1204, Arlington VA 22202-4302. Respondents should be aware that notwithstanding any other provision of law, no person shall be subject to a penalty for failing to comply with a collection of information if it does not display a currently valid OMB control number.

1. REPORT DATE **SEP 2009**	2. REPORT TYPE **N/A**	3. DATES COVERED **-**

4. TITLE AND SUBTITLE **Optical Measurements in Non-Equilibrium Plasmas and Flows**	5a. CONTRACT NUMBER
	5b. GRANT NUMBER
	5c. PROGRAM ELEMENT NUMBER
6. AUTHOR(S)	5d. PROJECT NUMBER
	5e. TASK NUMBER
	5f. WORK UNIT NUMBER
7. PERFORMING ORGANIZATION NAME(S) AND ADDRESS(ES) **The Ohio State University, Columbus, OH USA**	8. PERFORMING ORGANIZATION REPORT NUMBER
9. SPONSORING/MONITORING AGENCY NAME(S) AND ADDRESS(ES)	10. SPONSOR/MONITOR'S ACRONYM(S)
	11. SPONSOR/MONITOR'S REPORT NUMBER(S)

12. DISTRIBUTION/AVAILABILITY STATEMENT
Approved for public release, distribution unlimited

13. SUPPLEMENTARY NOTES
See also ADA562449. RTO-EN-AVT-162, Non-Equilibrium Gas Dynamics - From Physical Models to Hypersonic Flights (Dynamique des gaz non- equilibres - Des modeles physiques jusqu'au vol hypersonique)., The original document contains color images.

14. ABSTRACT

15. SUBJECT TERMS

16. SECURITY CLASSIFICATION OF:			17. LIMITATION OF ABSTRACT	18. NUMBER OF PAGES	19a. NAME OF RESPONSIBLE PERSON
a. REPORT **unclassified**	b. ABSTRACT **unclassified**	c. THIS PAGE **unclassified**	**SAR**	**52**	

Standard Form 298 (Rev. 8-98)
Prescribed by ANSI Std Z39-18

line shape, the very basics of which we present below (More detail can be found in many standard texts including [1,2,4,5] Very basically, the single photon allowed absorption of electromagnetic radiation is based on Beer's Law

$$\frac{I_t(\upsilon)}{I_o(\upsilon)} = \exp\left(-\kappa_\nu(\nu)L\right) \tag{1}$$

where $I_t(\nu)/I_o(\nu)$ is the ratio of the transmitted intensity, at the frequency ν, to the incident, L is the path length of the radiation through the absorbing medium, and $\kappa_\nu(\nu)$ is the absorption coefficient (with units m^{-1}) at the frequency ν, which is given by

$$\kappa_\nu(\nu) = \left[\frac{nB_{12}N_1h\nu_o}{c}\right]g(\nu-\nu_o) \tag{2}$$

In equation (2), B_{12} is the Einstein B coefficient for stimulated absorption, N_1 is the number density of absorbers in the lower quantum state (rotational, vibrational, and electronic) of the absorbing transition, and $g(\nu-\nu_o)$ is the spectral lineshape function. The relationship between the absorption coefficient, $\kappa_\nu(\nu)$, to what is known as the integrated absorption coefficient, is given by:

$$\kappa_\nu(\nu) = \left[\int\kappa_\nu(\nu)\right]g(\nu-\nu_o) \tag{3}$$

Note that the units of the integrated absorption coefficient, $\int\kappa_\nu(\nu)$, and spectral lineshape function are $m^{-1}-sec^{-1}$, and $1/sec^{-1} = Hz^{-1}$, respectively. At low static pressure conditions, on the order of a few torr or less, the spectral lineshape function is well approximated by the well known Doppler profile, given by

$$I(\upsilon) = \frac{1}{\Delta\upsilon_{D,HWHM}}\left[\frac{\ln 2}{\pi}\right]^{1/2}I_o\exp\left[-\frac{\ln 2(\upsilon-\upsilon_o)^2}{\Delta\upsilon_{D,HWHM}^2}\right] \tag{4}$$

where $\Delta\nu_D$ is the Doppler profile Half Width at Half Maximum, which is given by:

$$\Delta\upsilon_{D,HWHM} \equiv \left(\frac{\upsilon_o}{c}\right)\sqrt{\frac{(2\ln 2)k_B T}{m}} \tag{5}$$

where k_B is the Boltzmann coefficient, T is the static temperature of the absorbing medium, and m is the mass of the absorbing atom or molecule. The T dependence of $\Delta\nu_D$ forms the basis of the translational temperature measurement. The Gaussian behavior of the Doppler lineshape function is a direct result of the Maxwellian distribution for atomic/molecular speed, which couples to the wave equation for propagation of electromagnetic radiation via

$$E(t) = E_o\exp\left[-i(\omega_s t + \tilde{\mathbf{k}}\bullet\tilde{\mathbf{r}}(t)\right] \tag{6a}$$

$$\tilde{r}(t) = \tilde{v}_s t \Rightarrow \tag{6b}$$

$$E(t) = E_o \exp\left[-i(\omega_s t + \tilde{\mathbf{k}} \bullet \tilde{\mathbf{v}}_\mathbf{s} t)\right] \tag{6c}$$

$$E(t) = E_o \exp\left[-i(\omega_s + \omega_{Dop})t\right] \tag{6d}$$

where

$$\omega_{Dop} \equiv \tilde{\mathbf{k}} \bullet \tilde{\mathbf{v}}_\mathbf{s} \tag{7}$$

and the wave vector k is given by k = $2\pi n/\lambda$, where n is the medium index of refraction and λ is the radiation wavelength. Note, for simplicity, a constant amplitude (plane) wave is assumed. In equations (6), for the case of simple atomic/molecular absorption, E(t) can be thought of, somewhat simplistically, as the electric field "seen" by the absorbing atom or molecule which is translating through the trajectory r(t). Note that equation 6b requires that the atom or molecule translates at constant vector velocity, **v,** for a total displacement of many times the radiation wavelength. If this is the case then the absorbing frequency is shifted by the quantity ω_{DOP}, and the Maxwellian distribution of atomic/molecular speed gives rise directly to the Gaussian lineshape function, equation (5).

Note that while the discussion above refers to simple absorption (or fluorescence) only, a more general treatment of laser scattering (Rayleigh and Raman) is given in [6]. Finally note that when the atomic/molecular mean free path between collision is not much greater than the radiation wavelength, then a phenomenon known as "Dicke Narrowing" occurs [7]. A full discussion of this is beyond the scope of this lecture, but more detail on this and the similar phenomenal of rotational narrowing can be found in references [4, 8-11].

At higher pressures, in particular when the collision mean free path is much less than the radiation wavelength, the Doppler lineshape function is replaced by the Lorentzian "collisional" (also known as pressure) broadening lineshape given by

$$I(w) = \frac{I_o}{\pi}\left[\frac{\gamma_{coll}}{\left[(\omega - \omega_o)^2 + \gamma_{coll}^2\right]}\right] \tag{8}$$

where γ_{coll} is the collisonal broadening coefficient. Note that with the Lorentz function as defined in equation (8), γ_{coll} corresponds to the spectral Half Width at Half Maximum. In general, γ_{oll} is determined experimentally and given by an expression of the form

$$\gamma_{coll} = P\Delta\upsilon_{coll}(T) = P\Delta\upsilon_{coll,298}\left(\frac{298K}{T}\right)^x \tag{9}$$

For what is known as the hard sphere collision model, the exponent x is equal to 0.5, from simple kinetic theory. For most realistic inter-molecular potentials, the exponent x is in the range 0.5 – 1.0, with a value of approximately 0.7 being not uncommon.

At intermediate pressures (typically in the approximate range 0.05 - 0.5 bar for visible wavelengths), where neither Doppler nor pressure broadening predominate, the lineshape can in most cases be well approximated by a convolution of equations (4) and (8) known as the Voigt scattering profile, given by

$$I(\upsilon) = \left(\frac{\gamma_L}{\gamma_D}\right)\left(\frac{1}{\pi}\right)\left(\frac{\ln 2}{\pi}\right)^{\!\! 1/2} \int_{-\infty}^{\infty} \left[\frac{d\upsilon'}{(\upsilon - \upsilon_o - \upsilon')^2 + \gamma_L^{\ 2}}\right] \exp\left[-(\ln 2)\frac{(\upsilon' - \upsilon_0)^2}{\gamma_D^2}\right] \tag{10}$$

where, again, the line broadening coefficents are defined as Half Width at Half Maximum. Following the notation of Laufer [5], the Voigt profile can be written in more compact form as

$$I(\upsilon) = \left(\frac{B}{\pi\gamma_D}\right)\left(\frac{\ln 2}{\pi}\right)^{\!\! 1/2} \int_{-\infty}^{\infty} \left[\frac{e^{-y^2}}{(D-y)^2 + B^2}\right] dy \tag{11}$$

where

$$y \equiv (\ln 2)^{1/2}\left(\frac{\upsilon'}{\gamma_D}\right) \tag{12a}$$

$$B \equiv (\ln 2)^{1/2}\left(\frac{\gamma_L}{\gamma_D}\right) \tag{12b}$$

$$D \equiv (\ln 2)^{1/2}\left(\frac{\upsilon - \upsilon_o}{\gamma_D}\right) \tag{12c}$$

An example of the use of the Voigt profile will be presented below.

The determination of rotational temperature is based on simple statistical mechanics, specifically the use of the Boltzmann distribution for rotational energy [12]

$$f_J = \frac{(2J*1)\exp\left[\dfrac{-E_J}{k_B T}\right]}{q_{rot}(T)} \tag{13}$$

where $q_{rot}(T)$ is the rotational partition function and E_J is the energy of the Jth rotational quantum level, which for a rigid rotor wave function is given by $E_J = B(J)(J+1)$ where B is a constant. At room temperature, for simple diatomic molecules like O_2 and N_2, B, in cm^{-1} units is approximately two. Numerous diagnostic methods which utilize the rotational Boltzman distribution for determination of temperature exist in the literature, including, to name only a few, the use of diode laser absorption spectroscopy [13], two (or more) line Laser Induced Fluorescence [14], pure rotational Raman spectroscopy [15], and coherent Anti-Stokes Raman spectroscopy (CARS) [16]. Examples of the latter two methods will be presented below.

As a recent example of determination of translational/rotational temperature we cite the measurements of Parker, et al [17] who have performed tunable diode laser absorption spectroscopy (TDLAS) in the LENS 1 hypersonic facility, located at CUBRC in Buffalo, NY. TDLAS has experienced enormous growth in recent years due to the robustness and relative low cost of the instrumentation, and the inherently quantitative feature of absorption spectroscopy. In particular the technique has been used widely in combustion and sensor systems, a thorough recent review of which has been given by Allen, et al. [13]. LENS 1 is a hypersonic shock tunnel in which a driver/test gas is compressed to static temperatures as high as 8,000 K, and then expanded in an isentropic nozzle to velocities as high as ~ 4.2 km/sec [18]. The steady test time is on the order of several msec. The LENS diode laser work uses naturally abundant NO, formed

in the plenum of the hypersonic shock tunnel, as the absorbing molecule. As discussed in [17], non-equilibrium kinetic modeling had predicted NO mole fraction in the free stream LENS 1 flow as high as ~6%. The purpose of these studies was to quantify the actual NO concentration produced, as well as to serve as validation measurements for the computational predictions. Figures 1 and 2 show two typical single spectral trace diode laser absorption measurements, taken at 5 MJ/Kg and 10 MJ/Kg tunnel enthalpy conditions, respectively. Note that in both cases the data traces were obtained on a time scale of approximately 1 msec (1 kHz diode laser sweep rate). The two spectral absorption features coincide to a single, rotational transition within the fundamental vibrational band of the ground electronic state of NO, which exhibits a phenomenon known as lambda doubling [19]. Note that the lambda doubling fine structure splitting, ~0.01 cm^{-1}, is essentially completely resolved, a demonstration of the inherently high spectral resolution of the TDLAS approach. The fits to the data utilize the Voigt profile, equation (10), with the known free steam temperature and pressure as input data to a spectral modeling code based on the well known HITRAN data base [20]. Referring to equation (2), the HITRAN data base returns the equivalent of the value for the Einstein B coefficient, including rotational line strength factors, and values for the collisional (Lorentz) broadening coefficient at the free stream temperature. The free stream temperature is also used to determine the rotational Boltzman fraction for the chosen transition, which along with the ideal gas equation gives the value for N_1 in equation (2).
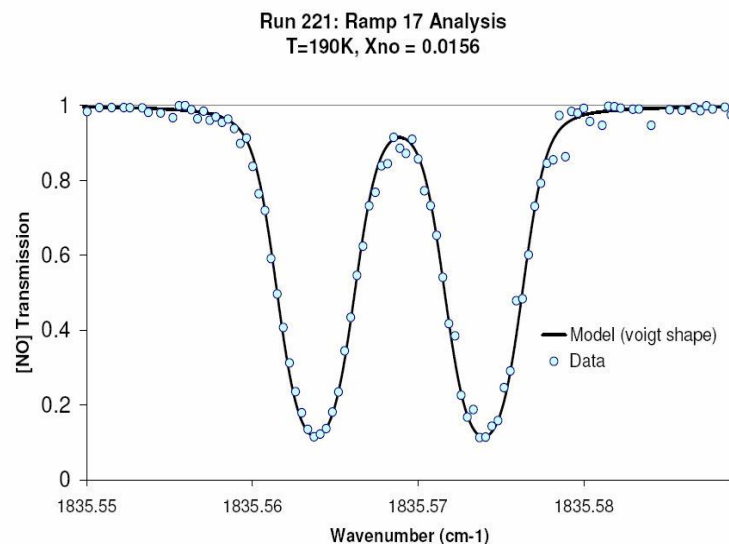

Figure 1
Single Trace TDLAS spectrum obtained in LENS 1 facility at 5 MJ/Kg enthalpy. From [17].
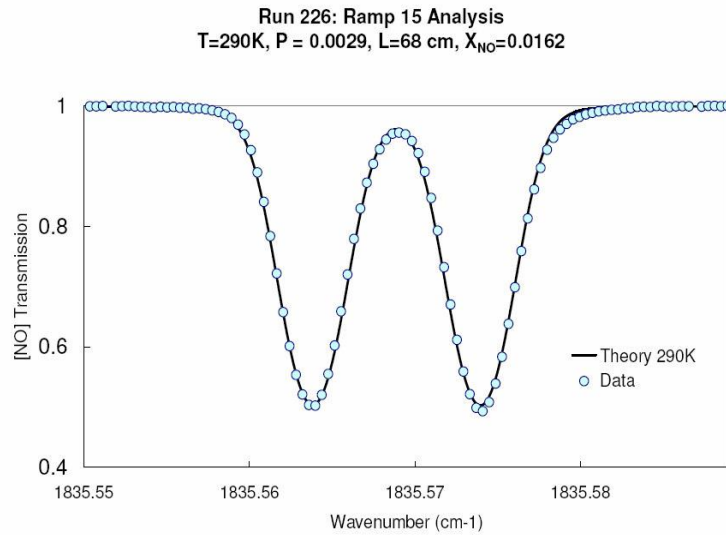
Figure 2

Single Trace TDLAS spectrum obtained in LENS 1 facility at 10 MJ/Kg enthalpy. From [17]

For the 5 MJ/Kg case (Fig 1), the temperature and NO mole fraction inferred from the best fit to the spectral model are 190 K and 0.0156, respectively. While the inferred temperature is in reasonable agreement with that calculated from non-equilibrium CFD codes, 229 K, the experimentally determined NO mole fraction is factor of approximately three less than the ~5% predicted from the calculations. For the 10 MJ/Kg case (Fig. 2), the experimentally inferred temperature and NO number density were 290 K and 0.016, respectively, as compared to CFD predictions of 563 K and 0.054. These discrepancies are a subject of on-going research.

Finally, it should also be noted that for the 5 MJ/kg condition the authors were able to make a novel measurement of rotational temperature, based on the known relative isotopic abundances of $^{14}N^{16}O$, the primary isotopomer, and $^{14}N^{18}O$ and $^{15}N^{16}O$. Each of these species exhibited a detectable absorption feature within the scanning range of the diode laser. Since the specific absorptions for each isotopomer corresponded to different values of rotational quantum number, the rotational temperature could be determined from the known isotopic abundances. The resulting value was 190 K, in excellent agreement with that inferred from the Voigt profile determination.

As a second example we cite the recent pure rotational Raman temperature measurements obtained in a laser pumped non-equilibrium oxygen containing plasma by Frederickson, et al. [21].   Raman scattering is a relatively simple optical diagnostic capable of quantitative determination of heavy species rotational/translational temperature, and vibrational distribution function of major species. Very basically (more detail can be found in [22] and [23]), scattering can be explained, classically, as the result of an incident electromagnetic wave inducing an oscillating electric dipole moment, p(t) which is given by the product of the polarizability, α, of the medium and the time-varying incident electric field ,E(t).

$$p(t) = \alpha \cdot E(t) \tag{14}$$

The polarizability is customarily expanded with respect to the vibrational normal coordinates (or "normal modes"), Q, of the molecule as

$$\alpha = \alpha_0 + \left(\frac{\partial \alpha}{\partial Q}\right)_0 Q + \cdots \tag{15}$$

where α_0 and $\left(\frac{\partial \alpha}{\partial Q}\right)_0$ are evaluated at the equilibrium internuclear displacement. Assuming harmonic oscillation of a single vibrational mode with natural frequency ω_k, so that $Q = Q_0 \cos(\omega_k t)$, and sinusoidal applied electric field, E, with frequency ω_l and amplitude E_o, the induced electric dipole moment is given by

$$p(t) = \left[\alpha_0 + \left(\frac{\partial \alpha}{\partial Q}\right)_0 Q_0 \cos(\omega_k t)\right] E_0 \cos(\omega_l t)$$

$$= \alpha_0 E_0 \cos(\omega_l t) + \left(\frac{\partial \alpha}{\partial Q}\right)_0 \frac{Q_0 E_0}{2} \left[\cos(\omega_l - \omega_k)t + \cos(\omega_l + \omega_k)t\right] \tag{16}$$

The first term in eq. (16) contributes to Rayleigh (and Thomson) scattering, and to pure rotational Raman scattering, an example of which will be given directly below. The second term represents vibrational Raman scattering, examples of which will be given in section 2.2.

In recent years, Rayleigh/Raman scattering has been augmented by the use of atomic/molecular vapor filters as narrow bandwidth filters and/or as spectral discriminators. The basic idea, illustrated in Fig. 3, is to utilize a narrow spectral line width laser which is tuned to a strong absorption resonance of the vapor. If a cell filled with the vapor is then inserted into the path between the scattering volume and the detector, elastic scattering can be attenuated while Doppler shifted and/or broadened scattering can be transmitted. In fact, the use of such vapor filters for Raman scattering dates to near the discovery of the Raman effect itself [25], although it is only with recent advances in laser technology that their true utility has been realized. In addition to continuous wave (cw) Raman instruments incorporating mercury vapor [26] and rubidium vapor [27, 28], the availability of high power, narrow spectral line width pulsed laser sources as common laboratory tools has enabled a wide range of new vapor filter-based scattering techniques. Most of these have utilized iodine vapor, which is particularly convenient because of strong absorption resonances within the tuning range of injection-seeded, pulsed Nd:YAG lasers, as well as the relative ease of filter construction, and availability of high quantum efficiency detectors, both for point measurements and for imaging. A recent special issue of the journal *Measurement Science and Technology* [29] contains a variety of molecular filter-based diagnostics, including velocity imaging, in which Doppler shifted Rayleigh or Mie scattering is converted to velocity by determination of the fractional transmission through a vapor filter, and temperature imaging, which is similar to velocity imaging but is based on Doppler broadening of molecular Rayleigh scattering, as opposed to Doppler shift. Other examples include: High Spectral Resolution Light Detection and Ranging (HSRL) [30] and, most recently, Thomson [31-32] and pure rotational Raman scattering [15], examples of both of which will be given in these notes.
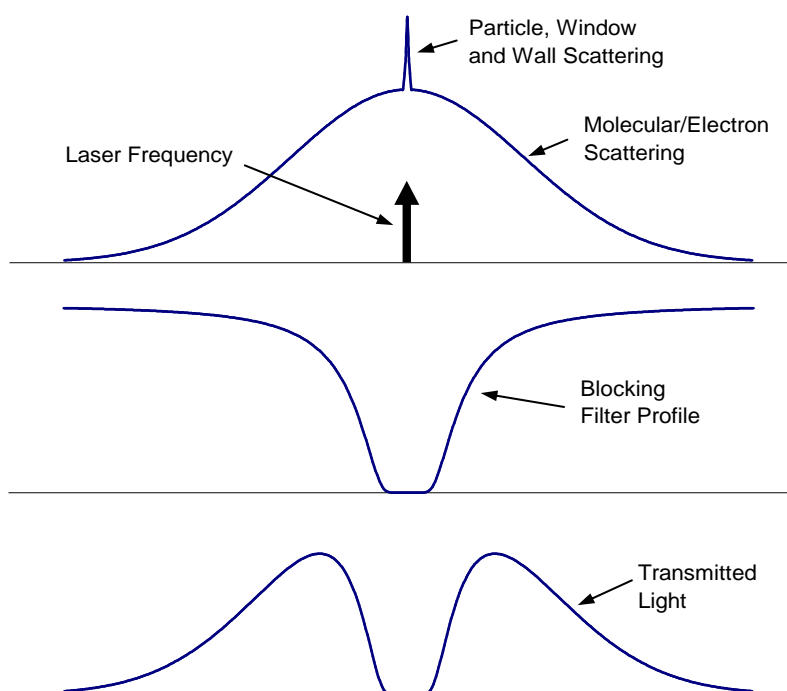
Figure 3

Basic Filtered Rayleigh Scatting concept

Figure 4 shows a filtered pure rotational Raman spectrum of N_2 at 500 torr and room temperature, using a pulsed titanium:sapphire laser – rubidium filter combination described by Lee and Lempert [15, 24]. As described in [15, 24] the effect of the filter was to reduce the intensity from stray light and molecular Rayleigh scattering by a factor as high as $\sim 10^6$, while transmitting greater than 80% of the rotational Raman scattering.
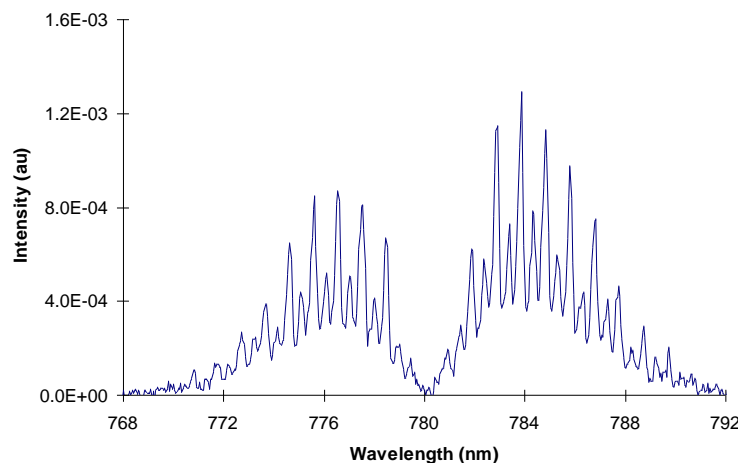
Figure 4

Pure rotational Raman spectrum of N_2 obtained with a rubidium vapor filter.

Filtered pure rotational Raman spectra, similar to that shown in Fig. 4, have been used by Frederickson, et al [21], and Lee, et al. [33] as part of a study of the influence of vibrational excitation on the low temperature rate of the three body free electron attachment to O_2 process

$$O_2 + e^- + M \leftrightarrow O_2^- + M \qquad\qquad\qquad (17)$$

These studies utilized the apparatus shown in Fig. 5a. A continuous wave CO laser creates a highly vibrationally non-equilibrium synthetic CO-seeded air mixture at ~1 bar pressure and room temperature, using a process known as Anharmonic V-V transfer [34], which will be described in more detail in section 2.2. The vibrational distribution functions (VDF) of all three components CO, O_2, and N_2, are determined from vibrational Raman scattering using an Nd:YAG laser (not shown in Fig. 5), typical results of which will also be shown in section 2.2. Rotational temperature is determined using a line narrowed titanium:sapphire laser, which is input collinearly to the CO laser, and can be translated radially with respect to the CO laser beam centerline in order to provide radially resolved temperature data. A pulsed electron beam is input to the non-equilibrium air mixture through a foil window, and time-dependent electron density measured using a simple microwave attenuation apparatus. Figure 5b shows typical results for rise and fall of the electron density for a 10 microsecond duration square primary electron beam current pulse. While not shown, when the CO excitation laser is not present, the electron density trace replicates precisely the 10 microsecond square e-beam pulse with no hint of the long, exponential decay (or rise) evident in Fig. 5b. From simple modeling, including both O_2 attachment, equation (17), and electron-ion recombination, which becomes the dominant process in the vibrationally excited medium, it is determined that the experimentally observed increase in the pulsed plasma lifetime is due to a five order or magnitude increase in the backwards, detachment rate of process (17), which results from vibrational excitation of M, the third body collision partner.
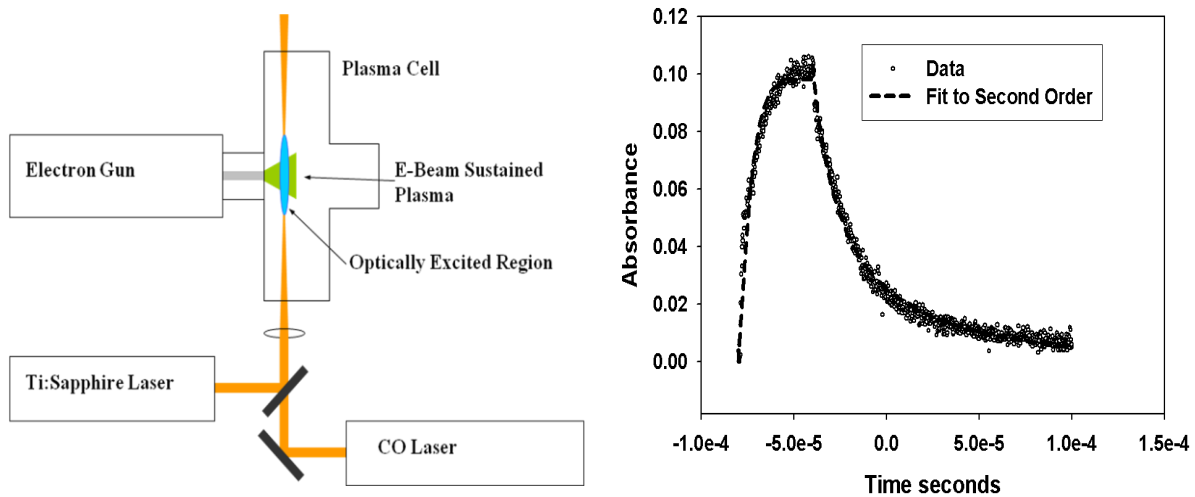
Figure 5
Apparatus (left) and typical time dependent electron density trace (right) from O_2 free electron attachment mitigation studies of Frederickson [21].

While the raw electron density data clearly showed complete mitigation of electron attachment, it was not clear whether this was truly a non-equilibrium effect, due to vibrational excitation, or a thermal effect, due to the known rapid increase in the reverse (detachment) rate of process (17) with increasing temperature. Figure 6 shows a filtered pure rotational Raman spectrum (S-branch only) obtained in-situe in the apparatus shown in Fig. 5a, in the presence of the CO excitation laser, along with a least squares fit. The resulting rotational temperature is 350 $\pm$ 7 K, ~300 K lower than that required to produce the long plasma lifetime observed in Fig. 5b, had the effect been thermal.
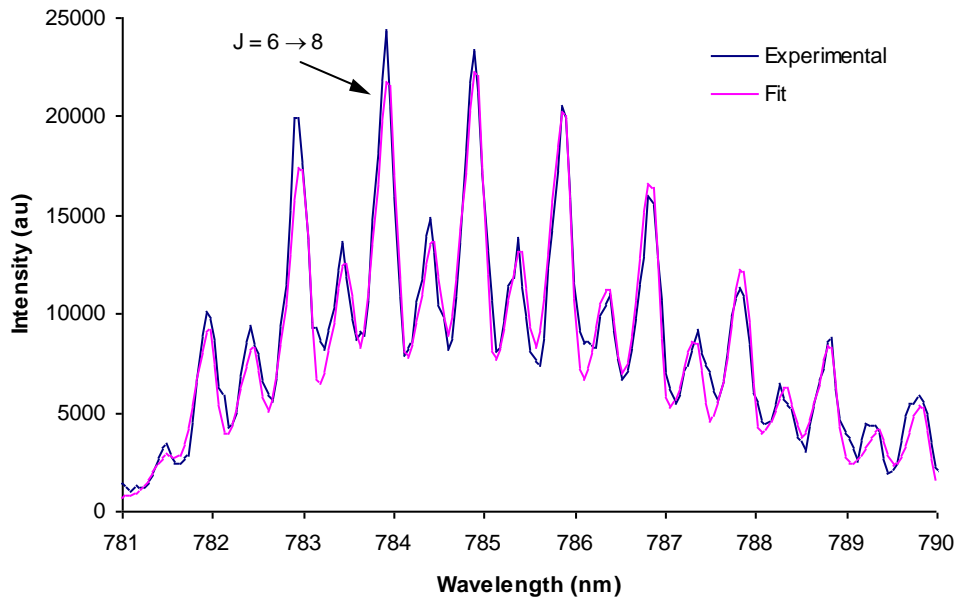
Figure 6

Filtered pure rotational Raman spectrum of optically pumped N_2/CO mixture at 1 bar pressure and least squares spectral fit. Inferred temperature is 355 ± 7 K. From [21].

As a final example of translational/rotational temperature measurements in plasmas, the recently developed coherent Rayleigh scattering diagnostic is cited [35, 36]. As illustrated on the left hand side of Fig. 7, coherent Rayleigh is a non-linear four wave mixing process, similar to coherent anti-Stokes Raman spectroscopy (CARS - which will be discussed in section 2.2), in which a pair of "pump" beams are overlapped in a fluid to form a traveling wave "grating" pattern similar to that from ordinary Laser Doppler Velocimetry. In this case the grating results from electrostriction, in which the traveling wave regions of high and low electric field induce a traveling wave density perturbation in the fluid. In essence extra molecules are trapped in the traveling wave potential well caused by the interference pattern from the two pump beams. If the amplitude of the potential well is not too large (ie, the laser beam intensities are not too high) than the molecules which become trapped are those which are already traveling with velocity near that of the grating. In other words, for weak fields, the pump laser beams do not greatly perturb the velocity distribution of the probed fluid. In it simplest configuration, scanning the frequency of one pump beam relative to the other causes the traveling wave velocity to be scanned. The relative scattering efficiency of the probe beam, as the traveling wave velocity is scanned, constitutes a measurement of the relative distribution of molecular velocity of the probed fluid molecules, ie the translational temperature. An example coherent Rayleigh spectrum, obtained from an argon glow discharge plasma at 50 mbar [36], is shown on the right side of Fig. 7. The inferred temperature is 479 ± 13 K. Note that this spectrum was obtained using a broad band pump beam, enabling "single shot" capability similar to that routinely employed for CARS. The spectrum was resolved using a Fabry-Perot etalon.
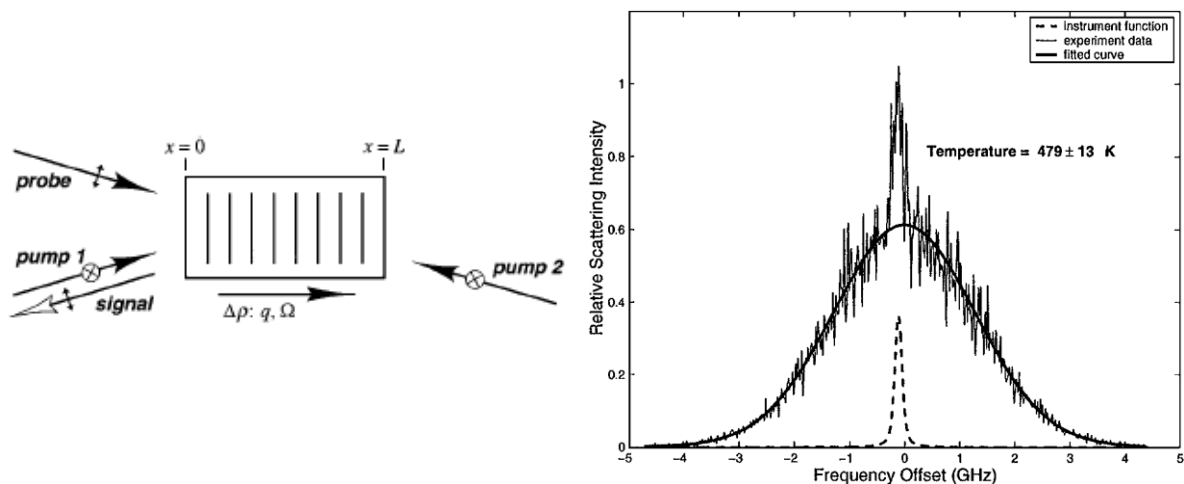
Figure 7
Schematic illustration of coherent Rayleigh scattering (left – from [35], and example
spectrum from argon glow discharge plasma at 50 mbar (right - from [36]).

2.2 Vibrational Distribution Function Measurements

Determination of the vibrational distribution function (VDF) is a central measurement requirement in non-equilibrium air flows and plasmas. In general, there are four common mechanisms by which the vibrational mode of constituent molecular species can be overpopulated. The first mechanism is the well known freezing of the thermal population formed in a high temperature plenum upon rapid supersonic/hypersonic expansion [37]. The second is due to quenching of electronically excited states, which can lead to highly vibrationally excited distributions in the ground electronic state. For example N_2 (A) state quenching, and the influence of this process on NO production in air plasmas, will be discussed in section 2.3. The third is the inherent non-equilibrium formed by resonant absorption of radiation, such as that from a CO laser [38]. Similar to resonant absorption, the fourth common mechanism of vibrational excitation is that due to electron impact excitation in plasmas and discharges which operate with an intermediate value of what is known as the reduced electric field, E/n. Briefly, more detail can be found in [39], the reduced electric field of a weakly ionized atomic/molecular plasma is a measure of the average kinetic energy to which a free electron in the plasma is accelerated in the interval between inelastic collisions with heavy species (A similar definition holds for fully ionized plasmas, but in this case the n refers to electron density). In general, the plasma E/n value correlates with the average electron temperature and electron energy distribution function (EEDF). Figure 8, taken from [39], illustrates this for air plasmas. Note that a common unit for reduced electric field is the Townsend, Td, which is defined at 10^{-17} V-cm^2. Typical weakly ionized diffuse "glow" discharges operate in the E/n range between approximately 10 and 100 Td. It can be seen, for example, that at an E/n value of ~100 Td, approximately half the energy deposited into the discharge results in electron impact excitation of the N_2 vibrational mode.

1: O₂ vibration
2: Rotation
3: Elastic Losses
4: N₂ vibration
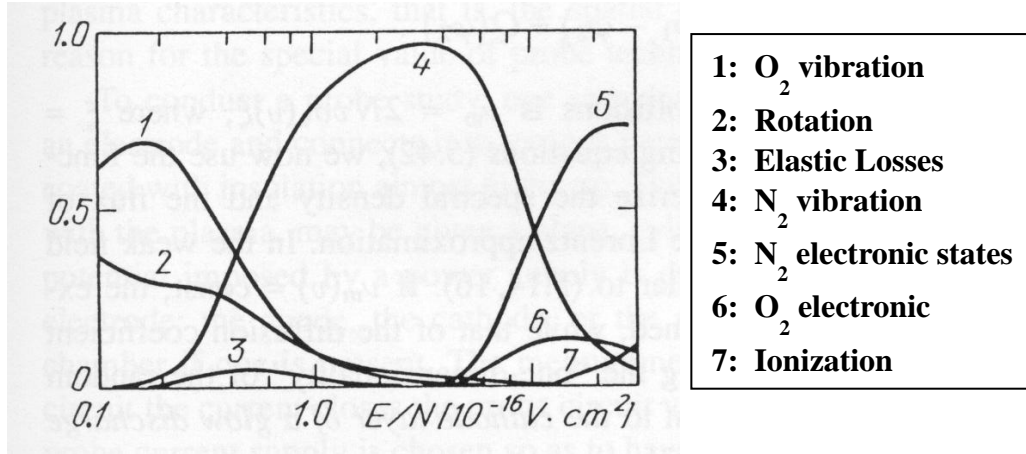**5: N₂ electronic states**
6: O₂ electronic
7: Ionization

Figure 8
Curve illustrating typical distribution of energy in air discharges between
internal modes as a function of E/n. Taken from [39].

It is well known that energy deposition into low vibrational levels of diatomic (and in many cases polyatomic) molecules leads to very substantial vibrational non-equilibrium due to a process known as anharmonic V-V energy transfer, the theory of which was initially developed to explain the mechanism of the population inversion in the CO gas dynamic laser [34]. Skipping the details, it can be shown from simple statistical mechanics that if the total number density of vibrational quanta for a particular vibrational mode, v_1, is held fixed in a fluid medium at temperature T, then the following distribution function, known as the Treanor, Rich, Rehm distribution, occurs

$$n_v = n_0 \exp\left[-(vE_1/k_B\theta_1) + (vE_1 - E_v)/k_B T\right] \quad (18)$$

where θ_1 is the characteristic temperature associated with the first level of the vibrational mode. Note that if T $\gg$ θ_1, then the distribution function given by (18) reduces to the Boltzmann distribution, since the second term in the exponential will become small. Note also that the second term

$$(vE_1 - E_v)/k_B T \quad (19)$$

depends only upon the ratio of the anharmonic contribution to the vibrational energy to $k_B T$. For harmonic oscillators, this term is exactly zero. As can be seen in Fig. 9, which gives plots of equation (18) for CO at several temperatures for the case $\theta_1 = 3000$ K (a typical value for simple diatomic molecules such as CO, N_2 and O_2), for temperatures below θ_1 the VDF becomes highly non-Boltzmann, and can even become inverted at high v. In practice, however, vibrational - translational energy transfer, the rate of which typically increases with increasing v, will truncate the VDF prior to achieving such an inversion.
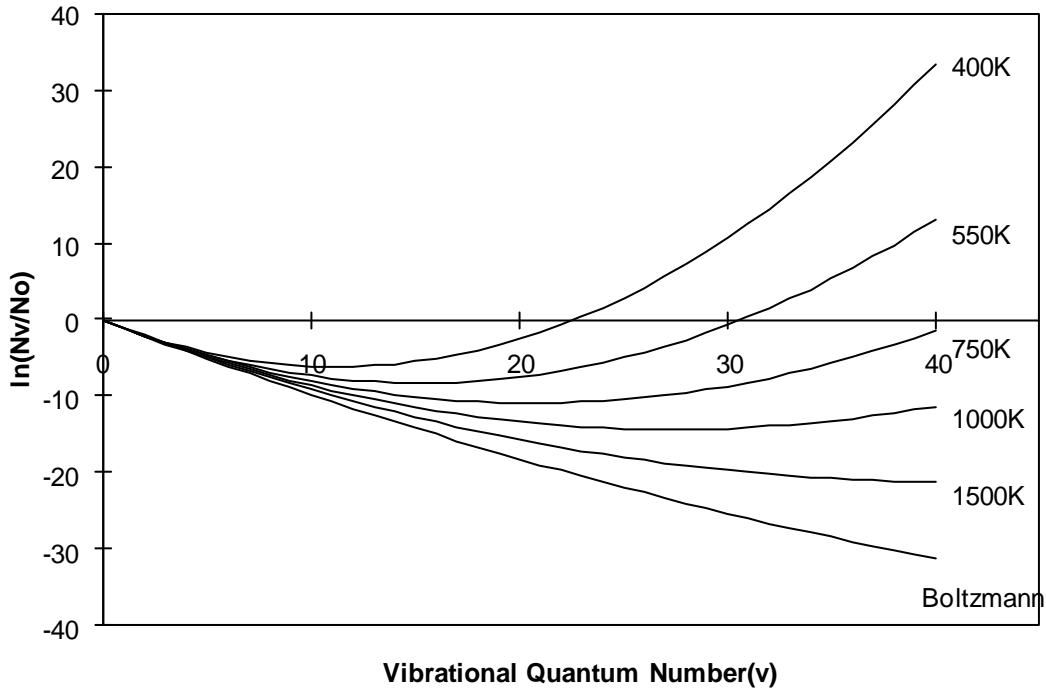
Figure 9

Calculated Treanor – Rich - Rehm distribution (equation 18) of CO at several values
of translational/rotational temperature. θ_1, the first level vibrational temperature, is
equal to 3000K.

As an example of this effect, Fig. 10 shows a spontaneous Raman spectrum, along with
corresponding VDFs, obtained from a highly non-equilibrium CO laser pumped plasma [38].
The gas mixture is 4% CO in N_2 at a total pressure of 410 torr. The plasma is created by resonant
absorption of CO laser radiation by the seeded CO, which in combination with the anharmonic
upward collisonal energy transfer mechanism described in the previous paragraph, produces the
highly vibrationally excited environment. Free electrons are then produced by the mechanism
known as associative ionization, in which two colliding molecules in high vibrational levels pool
their vibrational energy, for example

$$CO\ (v) + CO\ (v') \rightarrow [CO]_2^+ + e^- \tag{20}$$

In the specific case of CO the activation barrier for process (20) is ~6 eV, which is equivalent
to ~33 total quanta in the collision pairs. In Fig. 10 (left) each peak represents an unresolved Q-
branch Stokes Raman shift from a vibrational level with different vibrational quantum number. It
can be seen that significant population is observed in CO for levels up to v=37, and for nitrogen
for levels up to v=5. We point out that the achieving the observed fractional population of ~
0.001 for CO level v = 39 by equilibrium heating would require a temperature in excess of 15,000
K, whereas the observed temperature, based on rotation-vibration Raman scattering, was ~500 K
[38]. Of course at 15,000 K the mixture would be highly dissociated.
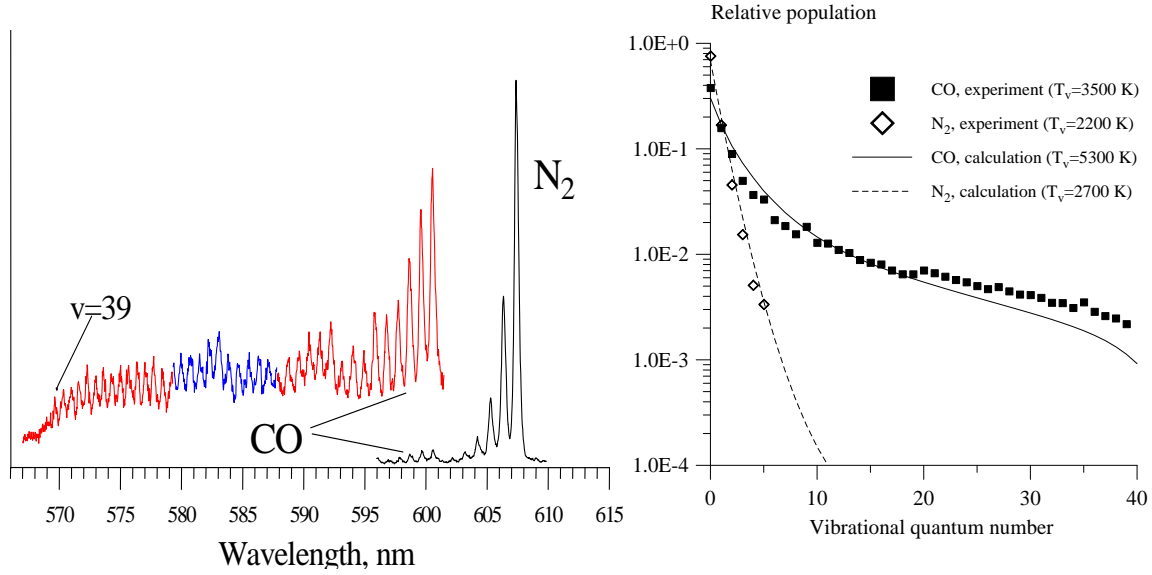
Figure 10

Experimental (left) spontaneous Q-branch Raman spectrum of CO laser pumped 4% CO in N_2 plasma, and (right) corresponding vibrational distribution functions and master equation modelling predictions. From [38].

The right side of Fig. 10 also includes the results of Master Equation modeling, which includes the effects of laser energy absorption, inter- and intra-species V-V transfer, V-T relaxation, and mass and thermal diffusion [38]. It can be seen that for this case, the agreement is quite quantitative. In this regard it is significant to note that Raman spectroscopy has the inherent advantage that inference of absolute population fractions is relatively straight-forward, although this requires consideration of the v level dependence of the Raman cross sections, which will be discussed in more detail below.

In oxygen containing mixtures there is more rapid inter-species V-V transfer between CO and O_2, due to its lower vibrational energy spacing. For CO laser pumped plasmas in CO seeded synthetic air, significant population was detected for levels as high as v=6 in CO and O_2, and v = 4 in N_2 [21, 38]. The vibrational temperature, defined in terms of the relative population of levels 1 and 0, exceeded 2000 K for each species, whereas again, the rotational temperature was ~500 K. It was this mixture which was used for the O_2 attachment mitigation studies discussed in the previous section.

Inference of absolute VDFs from Raman spectra requires that the vibrational level dependence of the Raman cross sections be known, since the observed Raman signal is directly proportional to the scattering cross section

$$I_{S,\parallel/\perp} = \left(\frac{d\sigma}{d\Omega}\right)_{\parallel/\perp} NI_{Laser} \tag{21}$$

where the parallel/perpendicular indices refer to polarization of the detected signal relative to that of the excitation laser. The vibrational dependence of Raman cross sections is discussed in some detail in [6]. Summarizing, for harmonic oscillator wave functions, vibrational Raman scattering cross sections scale exactly as v"+1 for Stokes ($\Delta v = +1$) scattering and v" for anti-Stokes $\Delta v =$

−1 [1].   Real molecules, however, exhibit anharmonicity which needs to be taken into consideration, particularly at high v. One approach is to utilize Morse potential wave functions, which result in the modified v-dependence [6]:

$$I_v \propto (v+1)\frac{(k-2v-1)(k-2v-3)}{(k-2v-2)^2(k-v-1)} \qquad \text{(Stokes)} \qquad (22a)$$

$$I_v \propto v\frac{(k-2v-1)(k-2v+1)}{(k-2v)^2(k-v)} \qquad \text{(ant-Stokes)} \qquad (22b)$$

where $k \equiv \omega_e/\omega_e x_e$ and where it is assumed that the polarizability derivative with respect to the vibrational mode, $\left(\frac{\partial \alpha}{\partial Q}\right)_0$ (See equation (15), is independent of v. In other words, all of the deviation from harmonic oscillator behavior in the Raman cross section is due to the quantum matrix elements for anharmonic oscillators.
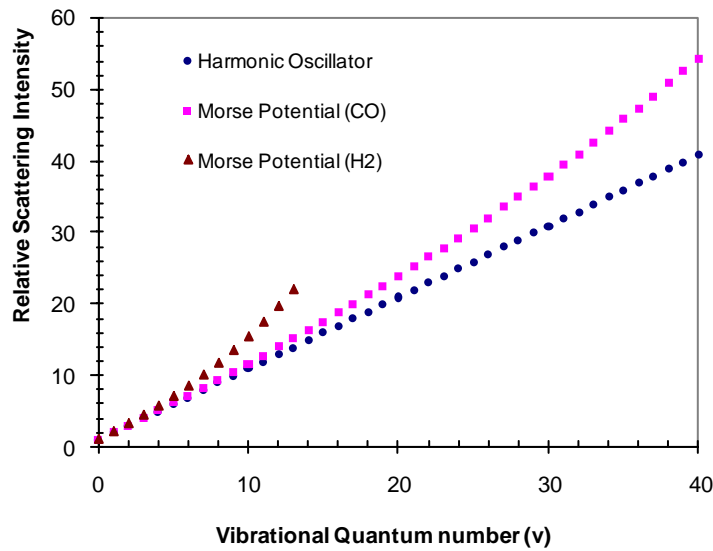

Figure 11
Relative scattering cross section as a function of v for harmonic
oscillator (●), CO (■), and H_2 (▲)

Figure 11 is a plot of the relative scattering cross section as a function of vibrational quantum number assuming harmonic oscillators (filled circles), and equation 22 for carbon monoxide (squares) and hydrogen (triangles). It can be seen that for v less than ~ 5, the anharmonicity correction is quite small, even for hydrogen which has the largest anharmonicity of any diatomic molecule. For carbon monoxide, which is representative of other common diatomic species, such as nitrogen and oxygen, the correction becomes appreciable (~7%) for vibrational levels exceeding ~ 10, and reaches ~33% at level v~40. As noted above, such high levels of CO have

been observed in optically pumped, as well as certain electric discharge, plasmas. In such cases, the anharmonicity correction to the vibrational cross sections cannot be ignored.

Similarly, Fig 12 shows the v-level dependence of the relative cross section for pure rotational Raman scattering which occurs due to rotation-vibration coupling. Specifically, the effect of increasing v is to increase the equilibrium internuclear separation, which in turns effects the angular momentum. This is expressed as

$$\beta_v = \beta_e + \beta_{e'} <r-r_e>_v + \frac{1}{2}\beta_{e''} <r-r_e>_v^2 + ... \quad (23a)$$

$$<r-r_e>_v = r_e \left[\left(\frac{3B_e}{\omega_e} \right) + \left(\frac{\alpha_e}{2B_e} \right) \right] \left(v + \frac{1}{2} \right) \quad (23b)$$

where α_e is the rotation-vibration coupling term used in the standard Dunham expansion for rotational energy. From Fig. 12, it can be seen that effect is minimal for typical diatomics such as N_2 (and O_2) and CO, but is quite significant for H_2.
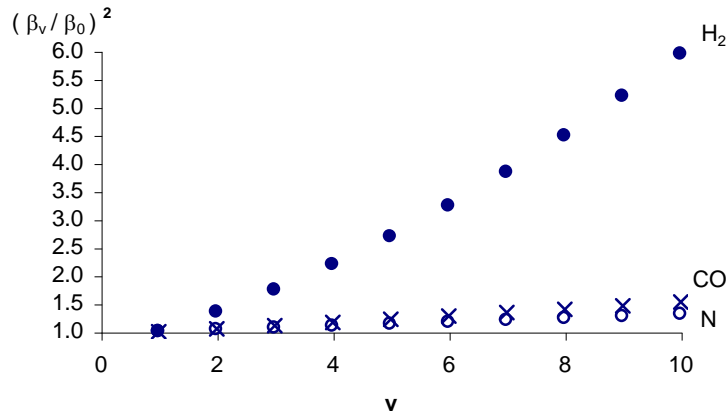

Figure 12
Vibrational level dependence of the square of the pure rotational Raman
cross section for H_2, CO, and N_2 [from 6].

Finally it is pointed out, for completeness, that for Rayleigh scattering equation (21) is in fact an approximation, albeit one which is valid under most applications of interest to the aerospace and aeronautics community. The exceptions occur when density fluctuations are correlated over a spatial dimension which is comparable to (or larger than) the reciprocal of the scattering wave-vector, such as at very small scattering angle and/or long wavelength light [40], or in the vicinity of critical points [41]. In these cases the Rayleigh scattering intensity is proportional to the square of the RMS fluctuation in the local density, which is in fact the general case for the intensity of Rayleigh scattering [42]. In most practical environments, where density fluctuations are due to random Brownian motion, these fluctuations obey Poisson statistics, such that δN^2 is proportional to N.

As a second example of significant vibrational non-equilibrium in air plasmas the recent CARS measurements of Messina et al. in nanosecond pulsed discharges is cited [43]. The purpose of these measurements is to explore, from a more fundamental perspective, the basic energy transfer processes which influence augmented flame properties, such as ignition delay

reduction and blow-off limit extension, which been observed in a number of recent studies of what has become known as Plasma Assisted Combustion (PAC). CARS is a well known [16] nonlinear Raman wave mixing technique which is in many respects similar to the coherent Rayleigh technique discussed previously. Referring to Fig. 13, taken from reference [43], a pair of pump beams and a Stokes beam are focused to a common cylindrical volume element in the medium to be probed, which in this case is a pre-mixed atmospheric pressure methane-air burner in which a pair of "point" electrodes is located downstream. A pulsed plasma is created between the electrodes by application of 10-40 KV – 70 nsec pulses, repeated at 100 Hz. Vibrational (Q-branch) CARS spectra, in air and in air-fuel mixtures, are obtained as a function of time delay after application of a discharge pulse.
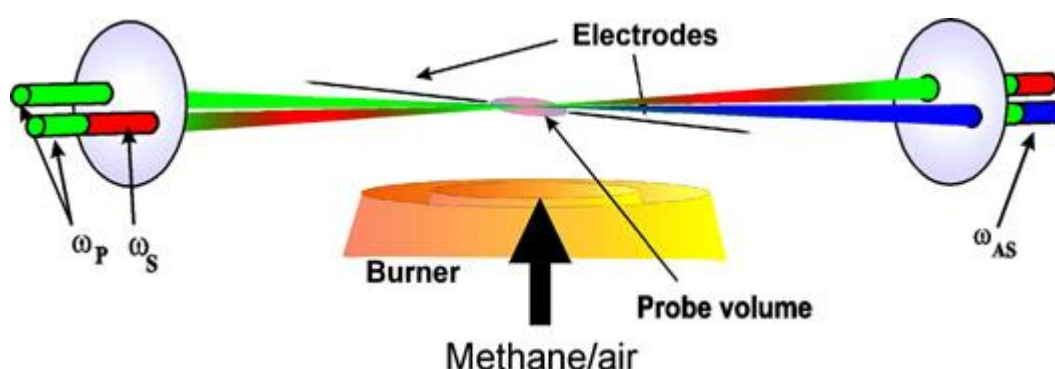

Figure 13
Schematic diagram of vibrational CARS measurement in nsec pulsed plasma burner.
From [43].

Figure 14 (left), taken from [43], shows an example single laser pulse CARS spectrum obtained in an air plasma (no fuel) 60 microseconds after application of the high voltage discharge pulse. It can be seen that a highly non-equilibrium environment has been created, with vibrational temperature of 1912 K and rotational temperature of 894 K. Note that the quality of the data is sufficient that the intensity can be given on a log scale. Based on histograms of single shot data, the authors give a stated statistical precision of ~100 to 150 K for both rotational and vibrational single shot temperatures, a value which includes a contribution from fluctuations in the discharge itself. The right side of Fig. 14 shows rotational and vibrational temperatures as a function of time after application of a single discharge pulse, for several values of discharge high voltage. Focusing on the vibrational temperature data, it can be seen that for both discharge voltages there is an initial decrease (between approximately 0.02 and 1 microsecond) in the vibrational temperature, which the authors attribute to vibrational quenching. For periods between ~1 and 30 microseconds an increase in vibrational temperature is observed, which the authors conclude may arise from vibrational excitation due to ion – neutral collisions [44]. In fuel-air mixtures, despite the more rapid energy transfer in collisions with CH_4, significant vibrational non-equilibrium is still observed, as can be seen in Fig. 15 which shows data similar to that of Fig. 14 for fuel lean (Φ=0.65) and rich Φ=2.2) mixtures.
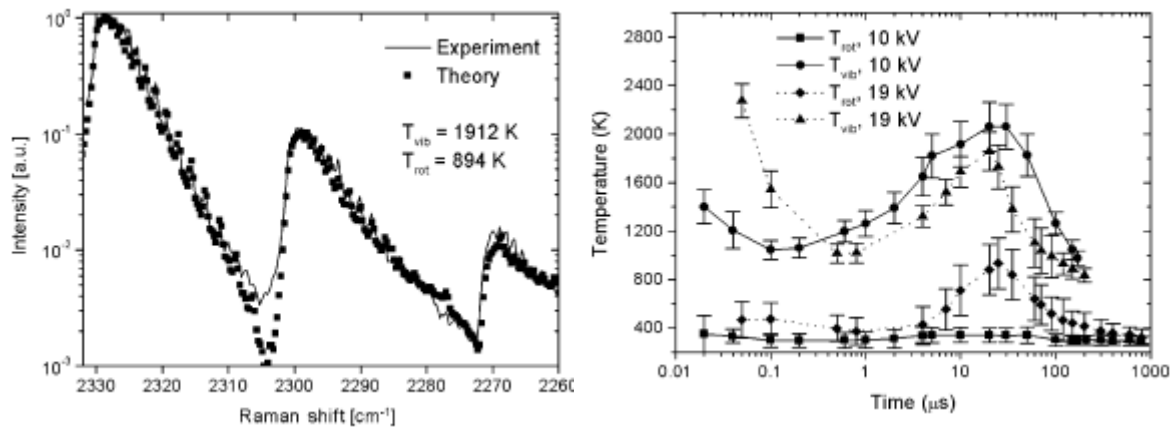
Figure 14
Single shot CARS spectrum (left) and temporal evolution of rotational and vibrational temperature (right) in nanosecond pulsed air discharge shown in Fig. 13. From [43].
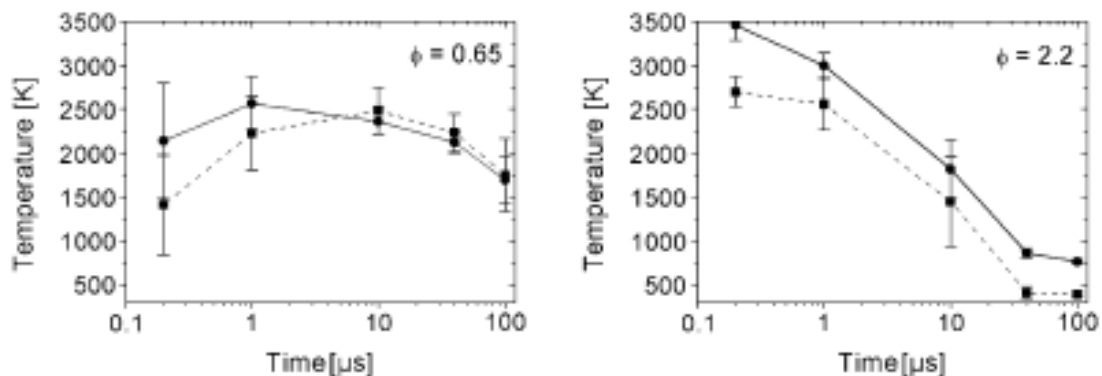

Figure 15
Temporal evolution of rotational and vibrational temperatures, as determined by CARS, in nanosecond pulsed methane-air mixtures. From [43].

As an example of a high speed nozzle expansion, we note the recent CARS measurements of vibrational temperature in the AEDC Hypervelocity Tunnel 9, located in White Oak, Md [45]. Tunnel 9 is an electrically heated pure N_2 blow down facility which is capable of operating in a range of Mach numbers from 7 to 14, with steady state test time in the range of a few tenths to approximately 15 seconds [46]. Motivated by some concerns between the lack of agreement

between experimental heat transfer data and computational predictions, a series of CARS diagnostics were performed to explore the possibility of vibrational non-equilibrium in the free stream test gas. Specifically, as described in [45], the numerical computations were found to over predict the observed heat transfer rate on a double cone model by approximately twenty percent. It was postulated that this differential could be due to vibrational freezing during the nozzle expansion, which would result in increased density and reduced velocity, respectively, as compared to an equilibrium expansion from the same plenum enthalpy. This would, in turn, result in a reduced heat transfer rate, since its value scales as ρu^3 [47].

Figure 16 shows typical N_2 vibrational Q-branch CARS spectra obtained from the free stream of the tunnel 9 facility at an operational Mach number of 10 (left) and 14 (right), respectively, along with spectral modeling corresponding to vibrational temperatures of 750 K and 1500 K, respectively. These values of vibrational temperature were determined from an inviscid, 1-D nozzle expansion code which includes finite rate kinetics for N_2 V-V transfer, the details of which are given in reference [45]. As can be seen in Fig. 16, however, no evidence of the predicted vibrational non-equilibrium is observed, which indicates the presence of rapid V-T relaxers in the nozzle test gas, most likely water vapor [48].
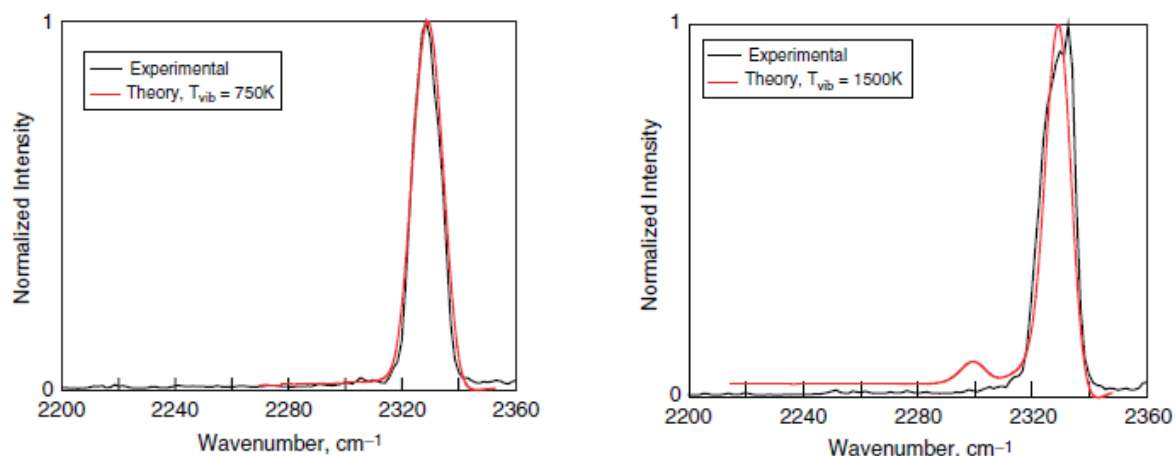

Figure 16
Experimental (black curves) and modelled (red curves) N_2 vibrational CARS spectra from tunnel 9 operated at Mach 10 (left) and Mach (14) right. The modelled vibrational temperature is based on the predictions of a 1-D non-equilibrium nozzle calculation. No evidence of vibrational non-equilibrium is observed. From [45].

A very different result was obtained in the recent spontaneous Raman measurements of Studer and Vervisch in the CORIA Inductively Coupled Plasma (ICP) wind tunnel [49]. Figure 17 shows a free stream Q-branch Raman spectrum obtained in air with the tunnel operating at a specific enthalpy of ~9 MJ-kg^{-1}. The rotational temperature is 2500 K, which corresponds to the equilibrium value, where as the vibrational temperature is considerably higher, 5200 K. Significant vibrational non-equilibrium was observed when measurements were performed in the boundary layer flow of a flat plate model under the same expansion conditions.
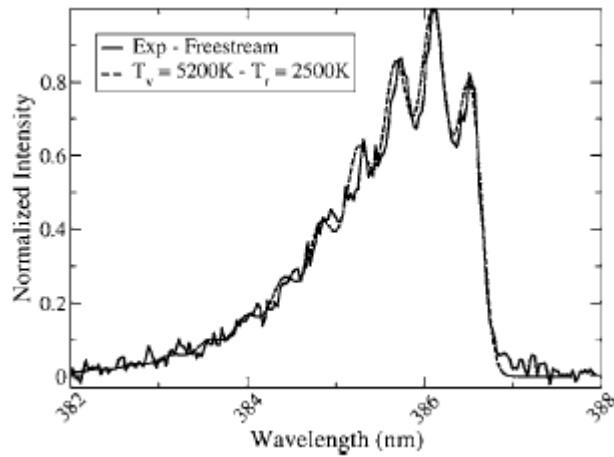
Figure 17
N_2 spontaneous Q-branch Raman spectrum from the free stream
of an inductively coupled plasma wind tunnel. From [49].

2.3 Meta-stable Electronic Non-Equilibrium Measurements

As can be seen from Fig. 8, increasing the E/n value of a discharge results in an increased fraction of the total energy being deposited into excited atomic and molecular electronic states. In this section we present some recent diagnostic measurements which probe two very important excited states of air species, N_2 (A $^3\Sigma_u^+$) and O_2 (a $^1\Delta$).

$$10.1\text{eV} \longrightarrow \text{C}(^3\Pi_u)$$

(2nd Positive)

$$6.8\text{eV} \longrightarrow \text{B}(^3\Pi_g)$$

(1st Positive)

$$5.7\text{eV} \longrightarrow \text{A}(^3\Sigma_u^+)$$

$$5.0\text{eV} \longrightarrow \text{NO (A)}$$
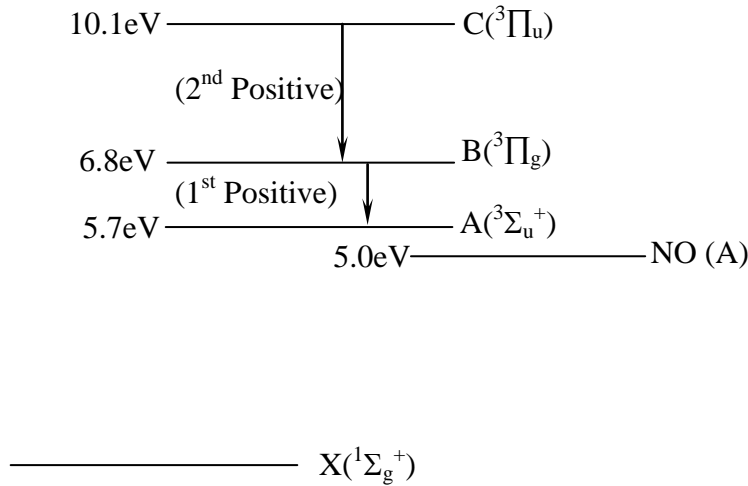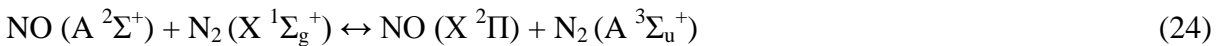
$$\text{X}(^1\Sigma_g^+)$$

Figure 18

Simplified energy level diagram showing N_2 excited electronic states of most relevance to air plasmas and non-equilibrium flows. NO (A), which is near resonant with N_2 (A) is also indicated.

Figure 18 shows a simplified energy level diagram illustrating the electronic states of N_2 which are, in general, of most relevance to typical non-equilibrium air plasmas. Note that the ground electronic state is a singlet, X ($^1\Sigma_g^+$), where as the other states represented have spin degeneracy three, A ($^3\Sigma_u^+$), B ($^3\Pi_g$), and C ($^3\Pi_u$). Spectroscopically, single photon transitions are strongly allowed between the C $\rightarrow$ B (2nd positive bands) and B $\rightarrow$ A (1st positive bands) states, but transitions from the A to X states are strongly forbidden (with spontaneous radiative lifetime of ~2 seconds). For this reason large meta-stable population tends to rapidly build-up in the A state, due to both direct electronic impact excitation, and radiative transfer from the higher C and B states. In addition due to a near energy resonance, there is rapid collisional energy transfer between the NO ($A\,^2\Sigma^+$) and N_2 A ($^3\Sigma_u^+$) states.

$$\text{NO (A }^2\Sigma^+) + \text{N}_2\,(\text{X }^1\Sigma_g^+) \leftrightarrow \text{NO (X }^2\Pi) + \text{N}_2\,(\text{A }^3\Sigma_u^+) \qquad (24)$$

There are a number of optical approaches which have been used to determine N_2 (A $^3\Sigma_u^+$) population. The most straight forward, albeit qualitative, is to take advantage of the reverse of reaction (24), and monitor NO (A $^2\Sigma^+$) $\rightarrow$ NO (X) (γ-band) spontaneous emission. As an example, Fig. 19 (left) shows typical NO emission spectra obtained as a function of time delay after initiation of a 20 nsec pulsed plasma, similar to that used for the studies summarized in the data of Figs. 14 and 15 [50]. In this case the plasma was initiated in air at P=60 torr. It can be seen that the NO γ (and β) band emission, for which the spontaneous radiative lifetime is on the order of 230 nsec, exhibits experimental radiative decay on a much longer, microsecond time scale. The right side of Fig. 19 compares the normalized time-dependent integrated emission intensity for this band system (in both air and 5% O_2 in N_2), obtained from spectra such as those shown in Fig. 19, with normalized N_2 ($A^3\Sigma_u^+$) population predicted by a kinetic model described in detail in [50]. Given the short NO γ-band spontaneous radiative lifetime, τ ~230 nsec, it is clear that the NO (A $^2\Sigma^+$) state is being "fed" by the metastable N_2 ($A^3\Sigma_u^+$) state, due to the rapid

reverse process of equation (24). In other words, in these systems the rapid quasi-equilibrium established between $N_2\,(A^3\Sigma_u{}^+)$ and NO $(A\,^2\Sigma^+)$ allows the approximate inference of one from the other.
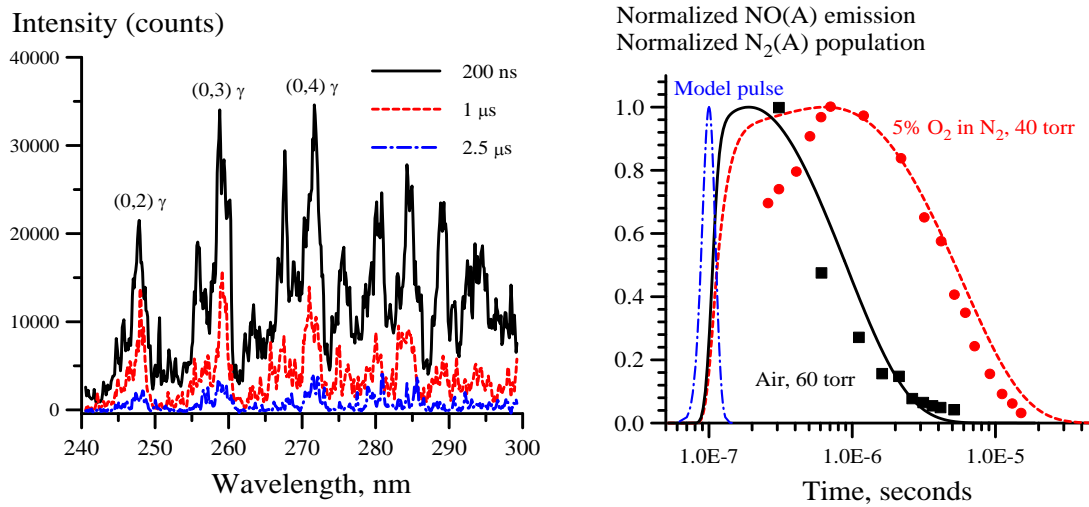

Figure 19

Typical NO emission spectra (β and γ bands) at different delay times after initiation of a 60 torr air- 20 nsec pulsed discharge plasma (left) and comparison with modelling predictions for N_2 (A) state population (right). From [50].

A more quantitative approach for determination of $N_2\,(A^3\Sigma_u{}^+)$ population is to use Laser Induced Fluorescence (LIF) [51]. LIF is similar to optical absorption except that re-emitted ("fluoresced") light is detected, typically at a 90° angle with respect to the laser propagation direction, rather than the transmitted laser beam itself [1]. LIF has the advantage that it can be extremely sensitive (order ppb in the case of strongly allowed transitions) due, principally, to the fact that the LIF signal, unlike that of absorption, is detected on a nominally zero background. The classic difficulty with LIF is the ability to quantify the measurement. While optical considerations, such as absolute collection efficiency of lenses, filters, and detectors, can typically be corrected for, there is an inherent problem in knowing the fraction of laser excited state molecules which are ultimately detected. This is known as the fluorescence quantum yield, a_{21}, given in somewhat simplified form by the expression

$$a_{21} = \frac{A_{21}}{\sum_i A_{2i} + Q + P} \qquad (25)$$

where A_{21} is the Einstein radiative decay rate for spontaneous emission between the laser populated level and the lower level of the fluorescing transition (or group of levels, in which case the subscript "1" represents a collection of levels), Q is the rate of collisional quenching, and P represents other non-radiative processes such as predissociation. The principal issue is typically the accuracy with which the collisional quenching rate is known, since this depends upon knowledge of the composition of the medium being probed, as well as the specific quenching rate coefficients for each of the components.

One approach for overcoming the quenching difficulty, applicable to low density fluids, is to temporarily resolve the detected fluorescence, from which the quenching rate can be experimentally determined. This method has been applied by De Benedictis and Dilecce [51] in numerous studies of low pressure pulsed N_2 and air RF discharges. The left side of Fig. 20 shows an example of such time-resolved LIF data applied to detection of N_2 $(A^3\Sigma_u^+)$ in varying vibrational levels. In the specific example shown in Fig. 20 N_2 (A) population in vibrational level 4 is excited to vibrational level 8 of the N_2 (B) state, using a Nd:YAG pumped dye laser at 595.9 nm. 1st positive band fluorescence down to vibrational level 5 of the N_2 (A) state is detected at 646.85 nm. Figure 20 shows three representative time-resolved traces corresponding to N_2 mixtures with 2%, 8%, and 20% oxygen, respectively, from top to bottom. Data such as this has been used to determine vibrational level dependent quenching rates for N_2 (A, v) by atomic oxygen and O_2 [51]. Data such as this is extremely important for understanding air discharge chemisty in that the N_2 $(A^3\Sigma_u^+)$ state is a precursor for many important processes, such as NO_x formation [50]. Indeed, several studies [52-54] have concluded that the following sequence of processes

$$N_2\ (A^3\Sigma_u^+)\ + O_2\ (X)\ \rightarrow\ N_2\ (X,v) + O_2(b^1\Sigma) \tag{26a}$$
$$N_2(X,v{\geq}12) + O\ (^3P)\ \rightarrow\ NO\ (X)\ +\ N(^4S) \tag{26b}$$

play an important role in NO formation in nonequilibrium air plasmas. A recent LIF study of NO formation in nsec pulsed plasmas by Uddi, et al. [50] reached a similar conclusion.
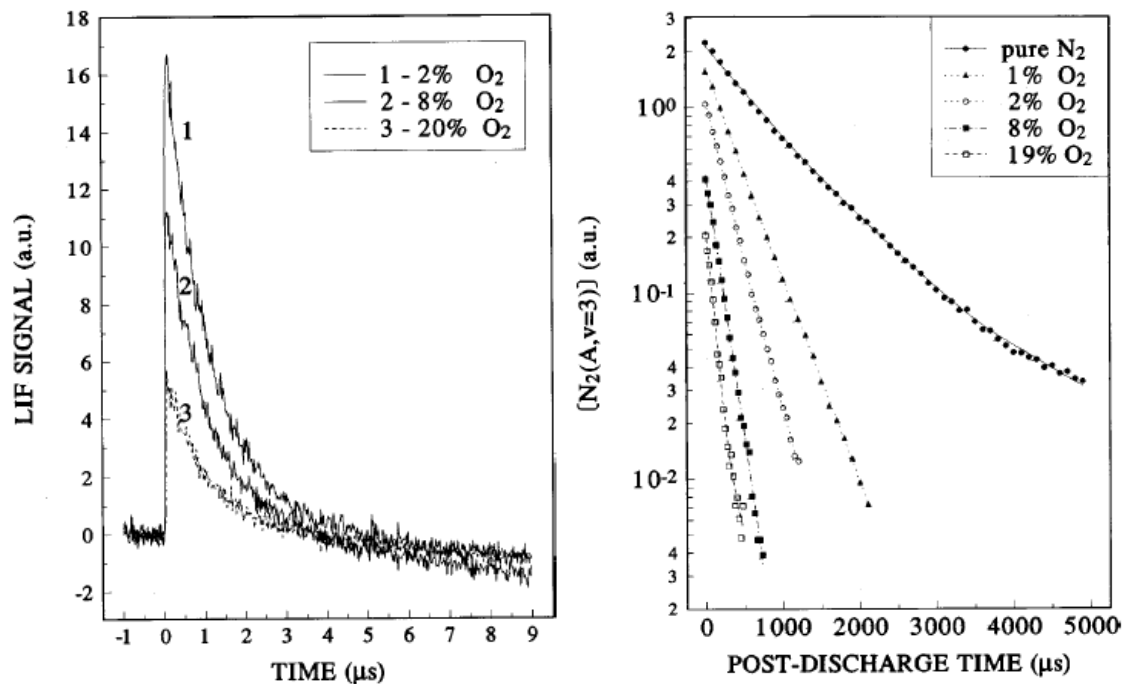
Figure 20
Experimental (left) time-resolved N_2 (A,v=4) LIF signal from pulsed 0.1 torr RF discharge
with several N_2:O_2 compositions, as indicated, and (right) typical N_2 (A,v=3) density
decay, from which O and O_2 quenching rate coefficients are inferred, obtained from the
LIF data. From [51].

At higher pressure, the LIF strategy outlined above for N_2 ($A^3\Sigma_u^+$) measurement loses
sensitivity due to the relatively slow radiative transition rate of the N_2 first postive band system,
coupled with the significant collisonal quenching rate of the upper B level [55]. To overcome
this difficulty Dilecce, et al have developed an optical double resonance strategy which employs
initial 1st positive band excitation, followed by a second excitation from the B to C states (2nd
positive band) [55]. Fluorescence has been detected from both the (2,1) band of the second
positive system, at 313.6 nm, and the (3,1) band of the 1st positive system, at 762.6 nm. The
technique has recently been applied to an atmospheric pressure NO seeded N_2 dielectric barrier
discharge [56].

As an alternative to LIF, Foissac, et al. [57] have recently reported an intracavity laser
absorption spectroscopy (ICLAS) diagnostic for N_2 ($A^3\Sigma_u^+$), using the apparatus shown
schematically in Fig. 21. ICLAS is one class of long path length absorption techniques which
take advantage of the inherently quantitative nature of absorption spectroscopy. A second such
approach, cavity ring down spectroscopy, will be described in section 2.4. ICLAS takes
advantage of the long "cavity lifetime" for photons which propagate between the mirrors of a
laser resonator. The key to the ICLAS method is that the absorbing medium is placed inside a
laser resonator cavity, which results in an effective absorption path length which is given by the
simple expression [57]

$$l_{eq} = \frac{l}{L} c t_g \qquad\qquad (27)$$

where l is the length of the absorbing medium itself (the microwave cavity in Fig. 21), L is the laser resonator path length (the distance between the mirrors), c is the speed of light, and t_g is what the authors term the "generation" time, between the onset of laser oscillation and recording of the absorption spectrum. The generation time is similar, but not identical, to the ring down time of a cavity, the difference being related to the fact that the ICLAS cavity exhibits photon gain as well as loss.
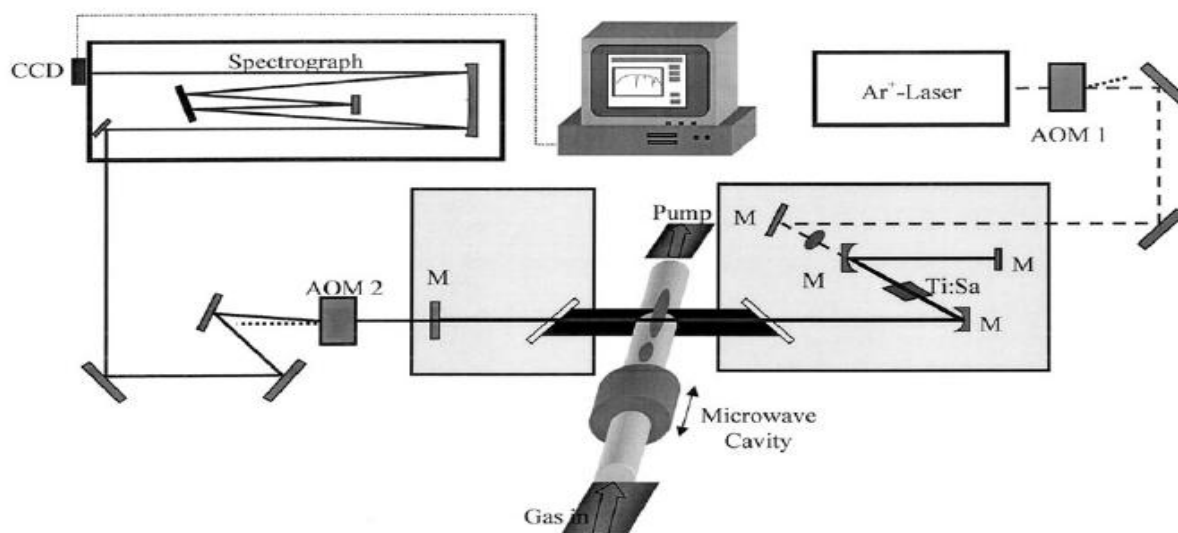

Figure 21
Diagram of N_2 (A) intracavity laser absorption diagnostic of Foissac, et al. (from [57].

Figure 22 shows an experimental ICLAS spectrum using the first positive band (A→B) in absorption. The upper spectrum was obtained with the microwave discharge located within the cavity, where as the lower spectrum was obtained by translating the cavity such that N_2 (A) was measured in the flowing afterglow of the discharge. In either case, absolute N_2 (A) density is inferred from the experimentally observed absorption via Beer's law (equation (1), where l_{eq} is used for the path length. N_2 (A) populations of between ~5 x 10^{10} and 5 x 10^{11} are reported [57].

Finally, measurement of N_2 (A) by cavity ring down spectroscopy, a technique which shall be described in more detail in section 2.4, has recently been reported by Stancu, et al [58] as part of a study of O atom formation and decay in nsec pulsed atmospheric pressure air discharges. Peak N_2 (A) density of ~2 x 10^{14} cm^{-3} was observed. More importantly a quantitative correlation was observed between the rise in O atom number density, measured by two photon LIF (to be described in section 3), and the fall in N_2 (A). This study confirmed that in high pressure, nsec pulsed air discharges a primary O atom formation mechanism, in addition to direct electron impact O_2 dissociation, is O_2 + N_2 (A) → O + O + N_2 (X).
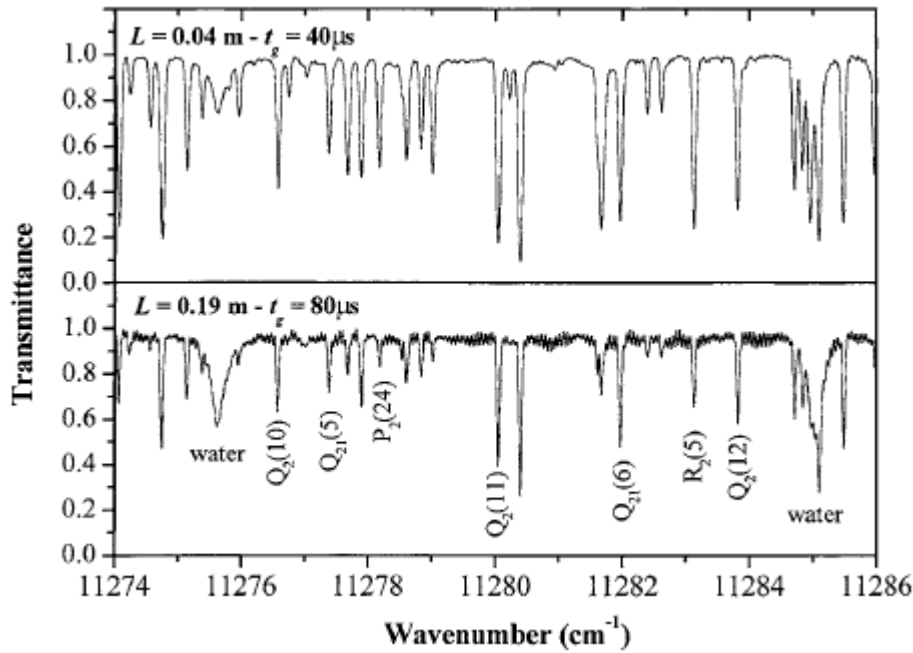
Figure 22
ICLAS spectrum of N$_2$ (A) state from microwave discharge. From [57].

As a second example of measurement of a metastable state of importance to air plasma chemistry some diagnostic approaches for O$_2$ (a $^1\Delta$) determination will now be discussed. Energy loading of the O$_2$ (a $^1\Delta$) state, whether by chemical reaction or by electric discharge (See Fig. 8), forms the basis for the gas dynamic oxygen iodine laser known as COIL (for chemical excitation) [59] and E-COIL (for excitation by electric discharge) [60-62]. Similar to the N$_2$ (A) state, O$_2$ (a $^1\Delta$) is extremely long lived, with spontaneous radiative lifetime of ~45 minutes. Nonetheless, despite this exceedingly slow radiative emission rate, spontaneous emission spectroscopy has been employed for determination of O$_2$ (a $^1\Delta$) state population in COIL and E-COIL studies [60-62].

Recently however an extremely sensitive long path length absorption approach has been developed for a more sensitive determination of O$_2$ (a $^1\Delta$) state population, based on a variant of cavity ring down spectroscopy known as Integrated Cavity Output Spectroscopy (ICOS) [63, 64]. Referring to Fig. 23, in the ICOS method a laser beam is injected off-axis into a high finesse cavity which contains the medium to be probed. Following the notation of [63] and [64], after transmission through the input high reflectivity mirror and propagation through the cavity the beam hits the second mirror, where most of it is reflected (since the cavity output mirror reflectivity is also high) and a small portion transmitted. Subsequent round trip propagation of the beam through the cavity results in a series of transmitted "beam spots" at the output cavity mirror, with transmission

$$I_1 = I_o T_1 T_2 e^{-\alpha NL} \qquad (28a)$$

$$I_2 = I_o T_1 T_2 R^2 e^{-3\alpha NL} \tag{28b}$$

$$I_3 = I_o T_1 T_2 R^4 e^{-5\alpha NL} \tag{28c}$$

$$I_{n+1} = I_o T_1 T_2 R^{2n} e^{-(2n+1)\alpha NL} \tag{28d}$$

where σ is the absorption cross section of the target species, N is the species number density, and L the separtion distance between the two mirrors (assuming the absorbing gas fills the cavity). A lens (on the right in Fig. 23) focuses all of the transmitted beams to a detector, which gives a total (the sum from all the beams) detected signal of

$$I_{Total} = I_o T_1 T_2 e^{-\sigma NL} \sum_{m=0}^{\infty} \left(R\, e^{-\sigma NL} \right)^{2m} \tag{29}$$

$$I_{Total} = \frac{I_o T_1 T_2 e^{-\sigma NL}}{\left(1 - R^2 e^{-2\sigma NL}\right)} \tag{30}$$

In practice, the species number density is found by determination of the ratio of the total detected signal with the cavity empty to that with the cavity filled with the absorbing species, invoking the relation

$$GA = \frac{I(\sigma NL = 0)}{I(\sigma NL)} - 1 \tag{31}$$

where A is the single pass absorption, 1-exp (-σNL), and G is the cavity path length enhancement factor, given by

$$G = \frac{R}{1 - R} \tag{32}$$

where R is the reflectivity of the mirrors (assuming both are equal). R, generally, is determined using the cavity ring down method, which will be discussed in section 2.4. For the instrument shown in Fig. 23, the enhancement factor is ~80,000, corresponding to an effective absorption path length of ~80 km.
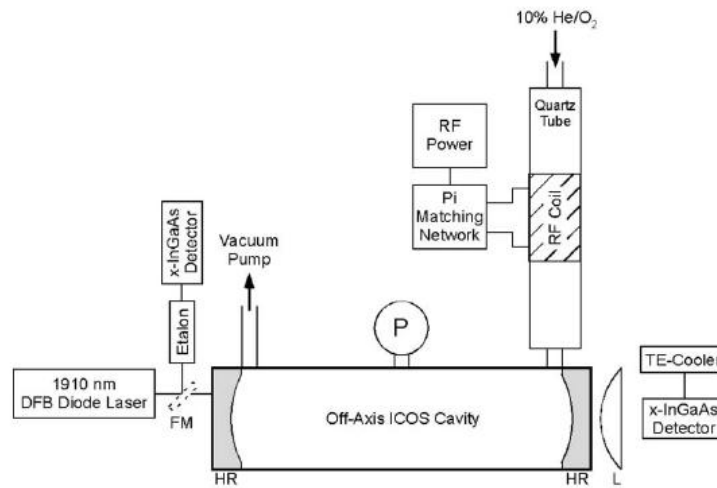
Figure 23
Schematic diagram of typical ICOS instrument. (from [64]).

As an example of the sensitivity of the ICOS method, Fig. 24 shows the cavity enhanced absorption from the Q(12) transition of the O_2 $b^1\Sigma_g^+ \leftarrow a\ ^1\Delta$ (Noxon band) where oxygen in the a $^1\Delta$ state was prepared in an RF discharge. Note that the transition is highly forbidden, with a spontaneous radiative decay rate (from b →a states) of 10^{-3} sec^{-1}. Despite the very low inherent absorption, the reported sensitivity, based on a S/N ratio of ~100 for spectra such as that shown in Fig. 24, is ~2.5 x 10^{13} cm^{-3} [64].
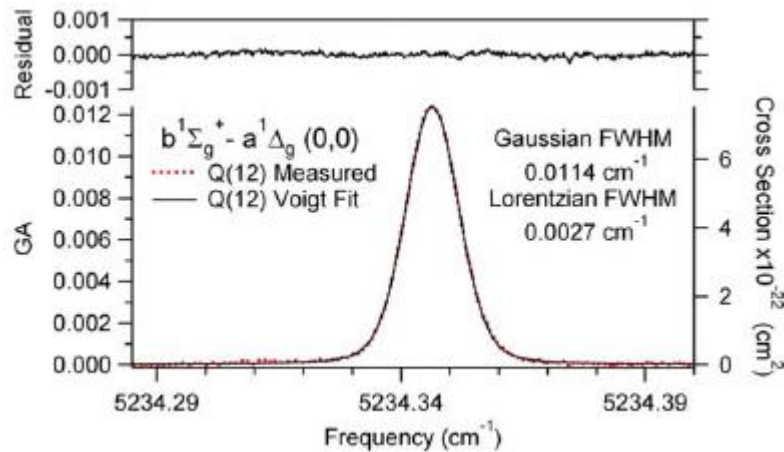

Figure 24
ICOS O_2 Noxon ($b^1\Sigma_g^+ \leftarrow a\ ^1\Delta$) band absorption spectrum, Q(12) transition. S/N is ~100, corresponding to O_2 (a $^1\Delta$) detection limit of ~2.x 10^{12} cm^{-3} per quantum state. From [64].

2.4 Positive Ion and Free Electron Measurements

The diagnostic literature on measurements of positive ions in non-equilibrium air plasmas is rather limited. However, Yalin, et al. have recently demonstrated both space-, and time-dependent measurements of N_2^+ in an atmospheric pressure glow discharge [65], and a nsec pulsed [66] plasma, respectively, using the Cavity Ring Down Spectroscopy (CRDS) technique. As illustrated in Fig. 25, CRDS is in many respects similar to ICOS, in that a high finesse optical cavity, which provides a long effective path length for species absorption, forms the basis of the method. In CRDS however, the laser is injected into, and propagates within, the cavity on-axis, with detection performed in the time domain. For a pulsed source, such as that used by Yalin, a small (but sufficient) fraction of the pulse energy enters the cavity, and propagates between the mirrors for a large number of passes, in a manner identical to ICOS. However, each time the pulse strikes the output mirror, a small fraction is transmitted to the detector. The detected signal decays exponentially in time (at least in the ideal case) according to [65]

$$S(t) = S_o \exp\left(-\frac{t}{\tau}\right) \tag{33}$$

where τ, the cavity ring down time, is given by [65]

$$\frac{1}{\tau} = \frac{c}{l}\left(\left[l_{abs}\kappa_\upsilon(\upsilon) + (1-R)\right]\right) \tag{34}$$

where $\kappa_v(\nu)$, again (See eqn. 3) is the absorption coeffient, and l_{abs} is the path length of the absorbing medium which is not, in general, the same as the distance between the mirrors, l.
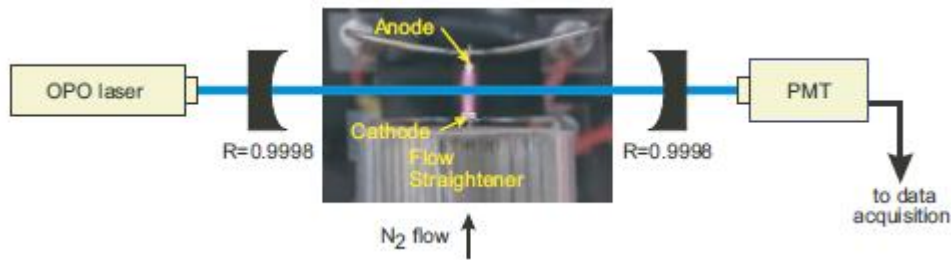

Figure 25
Schematic diagram of CRDS apparatus of Yalin, et al, used for N_2^+
measurement in atmospheric pressure N_2 plasmas. (from [65].

The measurement is performed by comparison of the ring down time, τ, when the absorbing medium is present within the cavity, to the ring down time, τ_o, when the cavity is empty. The presence of an absorbing medium causes the detected signal to decay more rapidly then the empty cavity case, specifically [65]
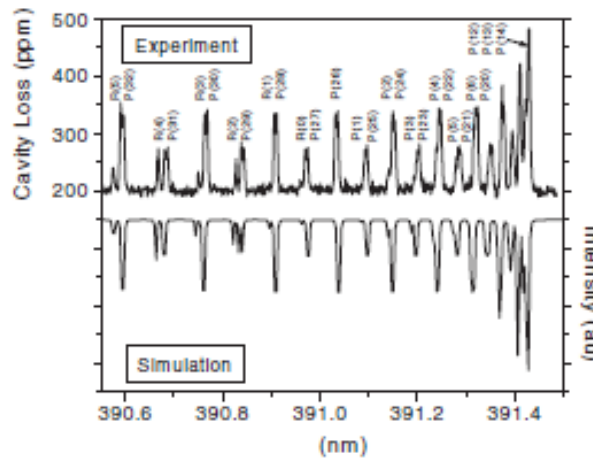
$$l_{abs}\kappa_\upsilon(\upsilon) = \frac{l}{c}\left(\frac{1}{\tau} - \frac{1}{\tau_o}\right) \tag{35}$$

CRDS is extremely sensitive due to both the long effective path length, and because the measurement is made in the time domain, rather than by measuring signal intensity. This is a significant advantage when using pulsed lasers where pulse to pulse energy fluctuations can be large, particularly for UV pulses which are formed from many non-linear harmonic and/or mixing steps.

Figure 26 shows an N_2^+ spectrum obtained by Yalin from the atmospheric pressure glow discharge apparatus shown in Fig. 25. The absorbing transitions are from the (0, 0) vibrational band of the B $^2\Sigma_u^+$ - X $^2\Sigma_g^+$ first negative system, with absorbing wavelength of ~391 nm. The UV wavelength is achieved by 2nd harmonic generation from the output of an Nd:YAG pumped Optical Parametic Oscillator (OPO). The inferred N_2^+ centerline concentration in the plasma, from spectra similar to that of Fig. 26, ranged from between 7.8 x 10^{11} cm^{-3} to 3.6 x 10^{12} cm^{-3}, dependent upon discharge current. Based on the observed S/N, the estimated detection limit is ~7 x 10^{10} cm^{-3}. It is noted that obtaining this sensitivity required careful attention to the specific design of the cavity. This important aspect of the measurement diagnostic is discussed in more detail by Spuler and Linne [67].

Yalin, et al., have also presented time-dependent measurements in an atmospheric pressure nsec pulsed N_2 discharge [66]. These measurements are performed by taking the time derivative of the ring down signal, so that [66]

$$l_{abs}\kappa_\upsilon\left(\upsilon,t\right)=-\frac{1}{c}\left(\frac{d}{dt}\left\{\ln\left[S\left(t\right)/S_o\right]\right\}-\left(1-R\right)\right) \tag{36}$$

Figure 26

Experimental N_2^+ CRDS spectrum from atmospheric pressure N_2 glow discharge (top), along with spectral simulation (bottom). From [65].

For completeness, we now discuss some recent advances in measurement of free electron density by Thomson scattering. Similar to spontaneous Rayleigh scattering, Thomson scattering results from laser induced polarization of charged species, principally, at least in weakly ionized plasmas, from free electrons. While the cross-section for free electron scattering is approximately one hundred times greater than that for Rayleigh scattering of common air species, the typically low free electron number density in weakly ionized air plasmas (~ $10^{10} - 10^{13}$ cm^{-3}) results in low scattering signals. In addition, because Thomson scattering in air plasmas (where T_e ~ 1 ev) occurs very close, spectrally, to the excitation laser frequency, it is very difficult to

sufficiently reduce the interference from stray scattering of the laser beam from window and wall surfaces using traditional grating based instruments.

One recently reported approach, employed by several groups, is based on the use of a custom fabricated triple grating spectrometer in which a physical block is used in place of the first exit slit to remove stray scattering at the laser wavelength. First developed by Noguchi, et al., [68], the technique has been further extended by Crintea, et al. [69], who have reported sensitivity as high as 2×10^{10} cm^{-3} for free electrons in an RF discharge with electron temperature of 2.5 eV. They also report, based on N_2 Raman scattering calibration, a system maximum sensitivity of 1×10^9 cm^{-3}. Note that achieving sensitivity of this order of magnitude requires signal averaging for 30 minutes (90,000 laser shots at 50 Hz repetition rate and 600 mJ per pulse at 532 nm).

A second recently reported approach uses atomic/molecular vapor filters, analogous to the filtered Raman (and Rayleigh) technique previously discussed (See Fig. 3, 4, and 6). The first reported system utilized a commercial Nd:YAG pumped dye laser in combination with a sodium vapor filter at ~580 nm [70], and shortly thereafter, independently developed rubidium vapor systems were also reported [15, 71]. Compared to rubidium-based systems, sodium systems have the advantage that the laser is relatively simple and is readily available commercially. The sodium vapor filter, however, is somewhat more complex to fabricate.

As an example of filtered Thomson scattering at low electron density [15], Fig. 27 shows a spectrum from a dc argon "constricted" glow discharge, obtained using the same instrument employed for the filtered rotational Raman spectra in Figs. 4 and 6. The argon pressure is 30 torr and the discharge current is 100 mamps. The constricted glow is ~1-2 mm in diameter and is stabilized by incorporation of a 500 ohm current limiting ballast resistor in series with the dc discharge. The left side of Fig. 27 shows the Thomson scattering signal superimposed upon the relatively large argon spontaneous emission, which is many orders of magnitude more intense despite employing a gated ICCD camera. The right side is a least squares fit of the experimental spectrum to a to a simple incoherent Thomson scattering model. The absolute intensity is calibrated using a N_2 pure rotational Raman spectrum similar to that of Fig. 4, taking advantage of the accurately known differential rotational Raman cross section of 5.4×10^{-30} cm^2/sr for the $J = 6 \rightarrow 8$ transition of nitrogen at 488.0 nm [72]. From this procedure the inferred values of electron number density and temperature are $2.0 \times 10^{13} \pm 6 \times 10^{11}$ cm^{-3} and 0.67 ± 0.03 eV, respectfully. Similar sensitivity, $\sim 10^{11}$ cm^{-3}, has been reported for the conceptually similar sodium vapor filter system [70]
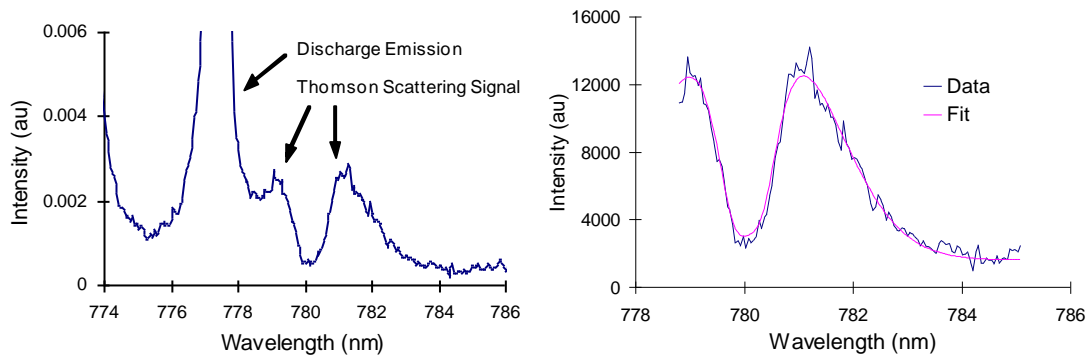
Figure 27

Rubidum vapor FTS spectrum from argon constricted glow discharge. Left spectrum illustrates scattering signal relative to spontaneous emission (despite utilization of gated ICCD detector). Right illustrates least squares fit to incoherent scattering model. From [15].

Miles, et al. [71] performed filtered Thomson scattering measurements in an atmospheric pressure argon lamp, using a rubidium vapor filter – titanium:sapphire laser combination similar to that used for Fig. 27. This measurement was complicated by the limited optical access of the lamp, which was solved by employing a 180° back-scattering geometry. Electron density and temperature of 1.61×10^{16} cm^{-3} and 0.82 eV, respectively, was reported.

3   An Integrated Diagnostic-Modeling Case Study: Plasma Assisted Combustion Kinetics at Low Temperature

The use of repetitively pulsed discharges has formed the basis for several recent studies of what has become known, somewhat generically, as Plasma Assisted Combustion (PAC) [73-79]. Specifically, using such pulsers, Kim et al. [73] have reported large increases in the critical co-flow velocity, V_{co}, leading to lift-off of a methane/air jet diffusion flame (from ~1-2 times the laminar flame speed, S_L, to as much as twenty times S_L). The same group has also observed increased NO production in premixed methane/air PAC flames, presumably due to excited metastable species reactions such as [74]

$$O + N_2^* \rightarrow NO + N \tag{37}$$

Similar stability limit extension has been reported by Pilla et al [75], who demonstrated significant reduction of the lean flammability limit in a premixed propane-air flame, down to $\Phi=0.3$. Several PAC studies have also been recently reported by the Starikovskii/Starikovskaya group [76, 77]. In particular, they demonstrated ignition delay time reduction, using a single high voltage, nanosecond duration discharge pulse, by more than an order of magnitude in argon diluted H_2/air mixtures preheated to ~900 K in a shock tube [76]. The same group has also observed an increase in blow-off velocity, by a factor of ~3 (from 3 to 9 m/sec), by application of a kHz pulse repetition rate nsec discharge to a pre-mixed, $\Phi=0.7$ argon diluted methane/air flame [77]. Finally, and of particular relevance to the study discussed here, Bao et al [78], and Lou et al

[79] have reported ignition and nearly complete combustion in low temperature oxidation of ethylene and methane in air at P=70-90 torr, at the conditions when the repetitively pulsed air plasma temperature (before fuel is added) was T=100-200^0 C.

Findings such as these have motivated a recent diagnostic and modeling study to explore fundamental low temperature plasma combustion kinetics in more detail [80, 81]. The study has been divided, broadly, into two sets of measurements, both of which utilized the basic "flow reactor" shown in Fig. 28. The apparatus consists of a single piece of rectangular cross section quartz channel, 150 mm long x 22 mm span x 10 mm height, with flanges at the ends for connection of the gas inlet and exit lines, and a test cell pressure sensor. The walls of the quartz channel are 1.75 mm thick. Two rectangular copper plate electrodes are attached directly to the outside surface of the channel and are covered by recessed acrylic plastic plates. The electrode plates are 14 mm wide and 63 mm long, and are rounded at the corners to reduce the electric field nonuniformity. The flow velocity is ~1 m/sec, corresponding to a residence time of the flow in the discharge region of approximately 0.08 seconds. Pulsed plasmas are generated using a pulser manufactured by Chemical Physics Technologies (CPT) which is capable of producing 20 kV pulses with individual pulse duration of ~25 nsec and maximum pulse repetition rate of 40 kHz.

The first element of the PAC kinetic study focuses on laser diagnostic measurements of key plasma and combustion species as a function of time after initiation of a single discharge pulse [80]. For these measurements the discharge is operated at 10 Hz, which both matches the repetition rate of the diagnostic laser and, more importantly, assures that each gas sample experiences only a single discharge pulse during its ~0.08 second residence time within the flow reactor. The first species which has been studied is atomic oxygen using the well known Two Photon Absorption Laser Induced Fluorescence (TALIF) method [82-84] where relative O number density vs time has been put on an absolute basis using a xenon calibration method described by Niemi, et al [85]. The method is similar to that previously utilized by Fletcher, [86], and Grinstead, et al [87], for measurements of N atom density in the NASA Ames Arc Jet.
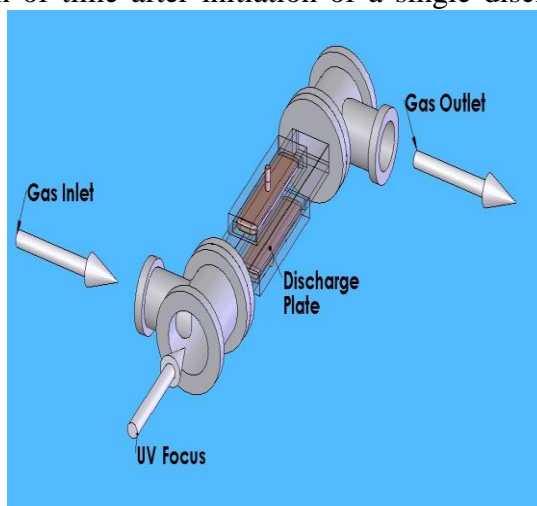

Figure 28: Optical access plasma flow reactor used for PAC kinetic studies.

The results of O atom TALIF measurements in air, and in methane-air and ethylene-air mixtures have documented in detail by Uddi, et al [80, 88] and will be only briefly summarized here. In particular Fig 29 shows results for air and methane-air (left), and air and ethylene-air at Φ=0.5 (right), both at 60 torr, along with modeling predictions using a 1-D plasma combustion kinetics code which has been developed as part of this study. The code, also described in detail by Uddi, et al. [80, 88] incorporates a set of ordinary differential equations for the number densities of neutral, charged, and excited species produced in the plasma, as well as the energy equation for prediction of the mixture temperature. This set of equations is coupled with the steady, two-term expansion Boltzmann equation for the electron energy distribution function (EEDF) of the plasma electrons, which yields the rate coefficients of electron impact processes by averaging the cross sections over the EEDF. Hydrocarbon chemistry is incorporated using both the GRI Mech 3.0 mechanism [89], and the recent mechanism of Wang [90] which

supplements GRI Mech 3.O with additional C_2 processes. In addition to equilibrium hydrocarbon chemistry, the OSU kinetic model incorporates chemical reactions of excited electronic species, electron-ion recombination and ion-ion neutralization processes, ion-molecule reactions, and electron attachment and detachment processes.

Focusing first on the air data (upper traces – black) of Fig. 29 (left – linear scale, right – log scale), it can be seen that to within the experimental precision the model agrees well with the experiment, correctly reproducing the peak O atom mole fraction of approximately $5 \cdot 10^{-5}$ (O atom number density of $1.0 \cdot 10^{14}$ cm^{-3}) and decay time (1/e) of ~2 msec. It should be noted, however, that the discharge reduced electric field, E/n, was treated as an adjustable parameter, varied to produce the best fit to the O atom air data. This best fit value of E/n (300 Td) corresponds to a total value of energy deposited into the plasma of 0.76 mJ, approximately half of which goes to O_2 dissociation. Sensitivity analysis showed that O atoms are primarily formed both by electron impact during the discharge pulse, $O_2+e \rightarrow O+O+e$, and by collisions of electronically excited nitrogen molecules with O_2 for times up to ~10 µsec after the pulse,

$$N_2\,(A^3\Sigma)+O_2 \rightarrow N_2(X^1\Sigma)+O+O \tag{38}$$

This initial rise after the discharge pulse can be seem more readily on the logarithmic scale plot. The dominant O atom decay process in air is recombination with oxygen resulting in ozone formation, $O+O_2+M \rightarrow O_3+M$, the rate of which, being unimolecular with respect to all minor species, is essentially independent of the discharge E/n.

The lower (red) left curve in Fig. 29 shows results of the air-methane mixture at an equivalence ratio of 1.0. Note that the modeling utilizes no adjustable parameters, other than the 0.76 mJ pulse energy obtained from the fit to the air data. It can be seen that both the data and model indicate peak O mole fraction which is comparable to that in air, but O atom decay rate which is increased by a factor of ~2-3. Sensitivity analysis shows that the increased atomic oxygen loss rate in methane-air occurs primarily due to reactions of H atoms and CH_3 radicals, which are generated by methane dissociation in the plasma, both by electron impact and by reactions with electronically excited nitrogen, principally

$$N_2(A^3\Sigma)+CH_4 \rightarrow N_2+H+CH_3 \tag{39}$$

Note that at low temperature the rate coefficient of the reaction between CH_4 and O at room temperature, $O+CH_4 \rightarrow OH+CH_3$, is very low, $k=4.8 \cdot 10^{-18}$ cm^3/sec, and does not contribute to the observed O atom decay. The significance of this, as compared to ethylene-air, will be now be discussed.

Figure 29
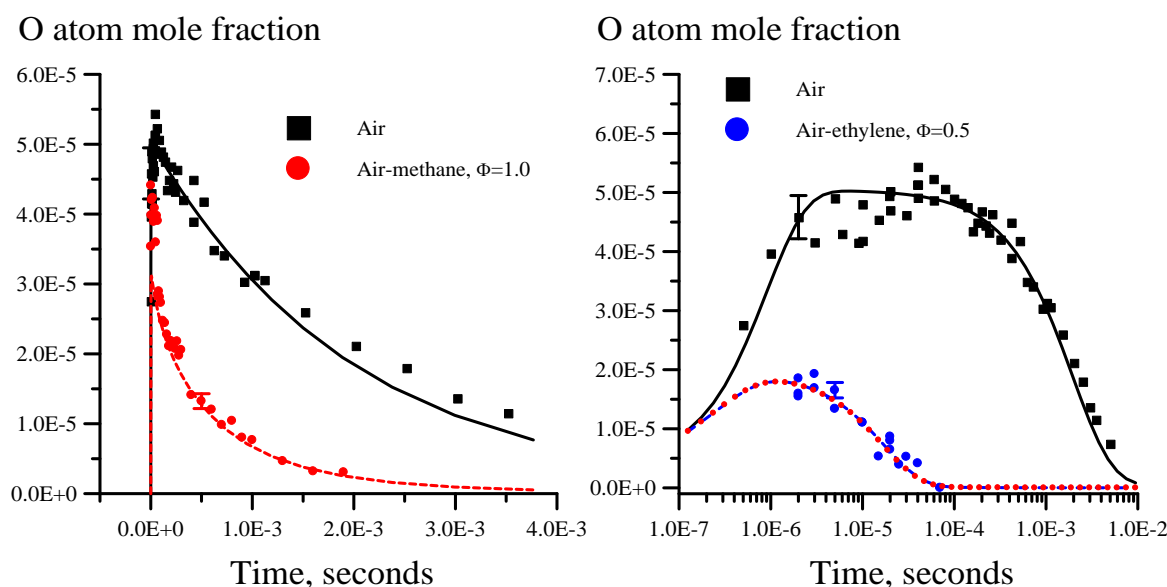
O mole fraction vs. time after a single high-voltage pulse in air (upper) and in a Φ=1.0 methane-air mixture (left) and Φ=0.5 ethylene-air mixture (right), both at P=60 torr, along with modeling predictions. (right). Air data shown on linear (left) and log (right) scales. From [80].

The lower (blue dots) right curve in Fig. 29 shows experimental O atom number density, along with predictions from the GRI Mech 3.0 (red dashed) and the Wang (blue dashed) ethylene oxidations mechanisms, both of which are essentially identical and predict significant deviations in both peak O mole fraction, and its rate of decay, when compared to air. Specifically observed and modeled peak O atom density is reduced by a factor of ~3 compared to air and, more significantly, the rate of decay is increased by more than two orders of magnitude, with lifetime (1/e) of ~20 μsec vs. ~2 msec. This rapid decay occurs because the rate of reactions between C_2H_4 and O atoms at room temperature, principally $C_2H_4+O \rightarrow CH_3+HCO$ and $C_2H_4+O \rightarrow CH_2CHO+H$, are fairly rapid, with k=4.9·10^{-13} cm^3/sec and k=2.6·10^{-13} cm^3/sec, respectively.

As discussed by Uddi, etl al. [80, 88] the low temperature reactivity of O and ethylene initiates a sequence of net exothermic oxidation chemistry which cannot occur in ordinary equilibrium combustion at these conditions. The resulting temperature rise further accelerates key oxidation processes, leading to ignition.

To quantify the above statement, Fig. 30 shows predictions from the Wang model of the total deposited discharge pulse energy and energy dissipated as heat in air, Φ=1 methane-air, Φ=1.0 ethylene-air, and Φ = 1.0 acetylene-air, all at 60 torr. It can be seen that in air up to 40-60% of the input pulse energy is stored in products (mostly ozone) of plasma chemical reactions and does not thermalize until ~1 sec after the pulse. In methane-air, ~2 msec after the pulse all input energy is thermalized because much less ozone is formed. Note that in this case methane oxidation results in a modest additional energy release, about 15% in excess of the input pulse energy. Finally, in ethylene-air (and acetylene-air) predicted additional energy release is significant, equal to 70% and 200%, respectively, of the input pulse energy. These results suggest that energy

release, accumulated over multiple pulses, may result in significant additional heating, particularly in ethylene-air and acetylene-air mixtures, leading to ignition. Indeed the modeling code predicts temperature rise by ~350 K for a 100 pulse "burst" in ethylene-air at Φ=1.0, as compared to less than 100 K increase for air.
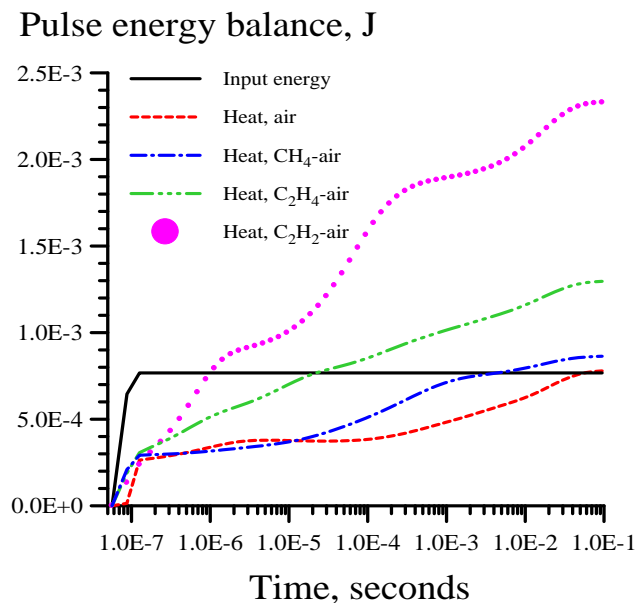

Figure 30: Input pulse energy and Wang model predictions for thermalized energy after a single high-voltage pulse in air, methane-air, ethylene-air, and acetylene-air mixtures at the conditions of Figs. 29. From [80].

The second element of the low temperature kinetics study, building upon the results

summarized above, focuses on burst mode ignition [81, 91]. For these measurements pre-mixed combustable mixtures flow through the discharge flow reactor at low velocity (~ 0.2-1 m/sec), as per the O atom measurements, but the discharge repetition rate is increased to ~20 – 50 kHz. OH, CH, and N_2 (2nd positive) spontaneous emission is obtained as a function of time with respect to the initial discharge pulse, using the same small monochromator used to capture O atom TALIF. As an example, Fig. 31 (left) shows OH emission (~309 nm) for 60 torr ethylene-air at Φ=1.0 and 40 kHz discharge repetition rate. While not evident in Fig. 31, due to the plotting resolution, for the first ~9 msec after the initial discharge pulse the OH emission falls to zero in the ~25 microsecond interval between the pulses (in fact the signal decays to zero in approximately 1 microsecond). At ~8 msec the OH signal during the individual pulses increases rapidly, and simultaneously does not fall to zero between the pulses (See the small "footprint" of emission which peaks at ~8.5 msec). These signatures (increase in OH emission during pulse and continuous emission in between the pulses) indicate that ignition as has occurred. Essentially identical signatures also occur in CH emission. Also shown are modeling predictions for temperature, obtained from the PAC kinetic code (validated by the previously described O atom measurements). It can be seen that the code predicts a rapid increase in temperature at precisely the time ignition delay time at which the OH emission spikes (and footprint appears).

By contrast, the right side of Fig. 31 shows N_2 (C-B) emission for air (upper blue curve) and ethylene-air at the same conditions as that of the left. Again, for both air and ethylene-air, the N_2 emission appears (at higher plotting resolution) as a series of approximately constant amplitude spikes corresponding to the individual pulses, and falls to zero in between them. Unlike OH and CH, there is no continuous "footprint" emission in between the pulses.
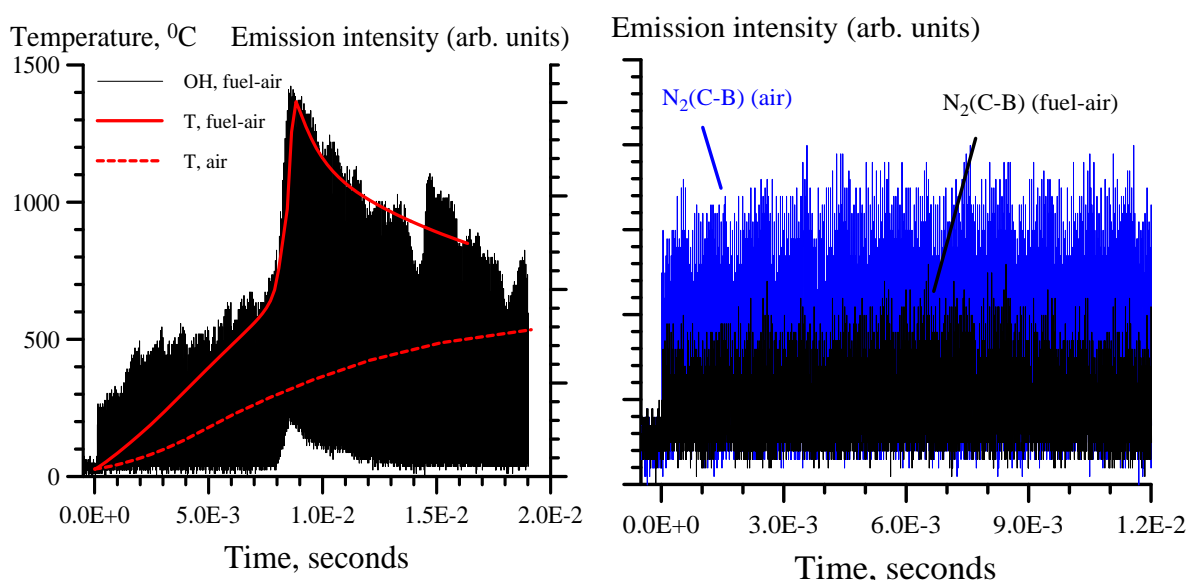

Figure 31
Experimental OH (left) and N_2 (right) emission as function of time after initiation of discharge pulse burst at 40 kHz repetition rate and 1 m/sec flow velocity. OH curve has modelled temperature from kinetic model superimposed. From [91].

The results of Figs 30 and 31 clearly point to exothermic plasma chemical oxidation reactions, initiated by O, H, CH_3 etc. electron impact radical formation by the pulser, which produce thermalized energy in excess of that input directly from the discharge, resulting in

sufficient heating to produce ignition. However, the question remains as to whether the observed ignition is due only to excess heat generation, or is there an additional effect due to "active" species generated by the plasma?

To explore this possibility, Fig. 32 shows two predicted temperature temporal profiles corresponding to ignition of a 60 torr Φ=1.0 ethylene-air mixture and 50 kHz discharge repetition rate. The lower (red) trace is the prediction from the full PAC kinetic modeling code and indicates a slow temperature rise for ~6 msec, followed by a rapid temperature spike, indicating ignition. This curve is similar to the temperature curve of Fig. 31 except that at the higher discharge repetition rate, 50 vs 40 kHz, ignition occurs with shorter delay (6 vs 8 msec). The upper (blue) curve shows the temperature prediction from the Wang equilibrium chemistry model, with heating rate input as an adjustable parameter. In this case, the heating rate is constant in time and has been adjusted to produce ignition at the same 6 msec delay as that predicted by the full PAC code. It can be seen that PAC ignition occurs at a temperature (~660 ^{o}C) which is more than 300 degrees lower than that for equilibrium oxidation chemistry (~970 ^{o}C).

Similar modeling. shown on the right side of Fig. 32, has compared ethylene-air PAC ignition delay with equilibrium heating ignition delay for the case where the heating rate is adjusted to result in ignition at the same temperature (~ 670 ^{o}C). As can be seen, in this case, PAC ignition was predicted to occur with delay time almost two orders of magnitude less than that for equilibrium oxidation chemistry (8 vs 600 msec).
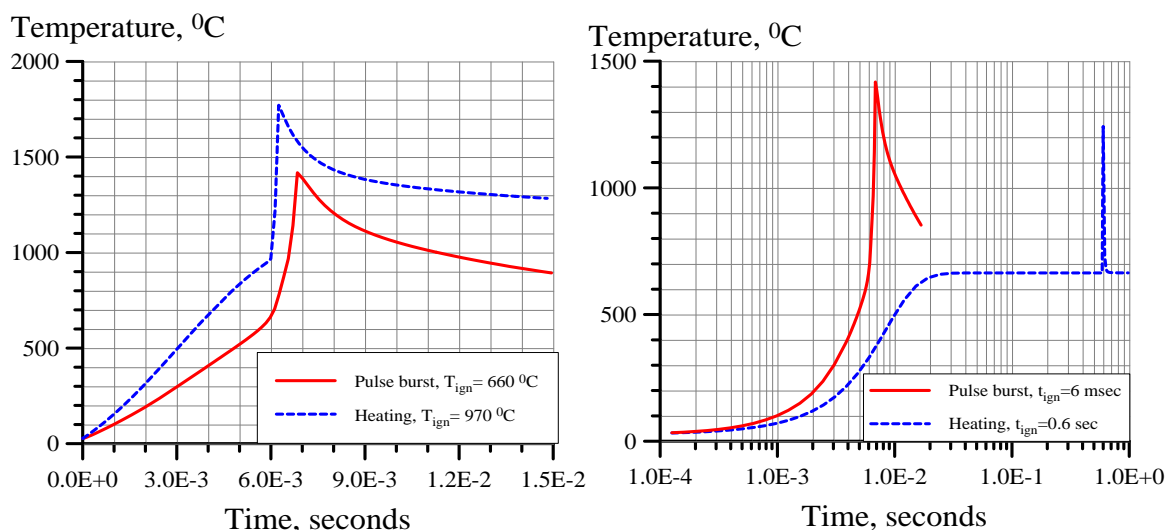
Figure 32

Modeling cmparison of ignition temperature (left) and ignition delay (right) for 50 ethylene-air repetitively pulsed plasma at 50 kHz. Red curves use full OSU PAC kinetic code, whereas blue are predictions for thermal, equilibrium heat addition.

4   An Overview of Recent Progress in Ultra High Frame Rate Imaging

Laser-based optical diagnostics, such as those cited in sections 2 and 3 of this lecture, are now relatively commonplace in fluid and combustion laboratories worldwide. Inherent to all of the cited techniques, however, is a trade off between spatial and temporal resolution. Planar imaging technique are clearly capable of simultaneously acquiring data at multiple points within a flow or combustor, but require high energy pulsed lasers to produce sufficient intensity within the object plane. Repetition rates for such lasers are typically limited to the order of 10 to 100 Hz. Supersonic/hypersonic flow fields, however, are characterized by turbulent, and/or unsteady features with frequency of 10s to 100s of kHz. In addition, many supersonic/hypersonic test facilities, such as LENS, operate with steady state test times of order a few milliseconds, or less. Clearly the capability of obtaining multiple planar images within a single run of such a facility would greatly enhance the information which can be obtained in the limited number of runs typical of a given hypersonic test program.

In response to this need we, and others, have been developing the capability of generating "trains" of 20-30, high-energy Nd:YAG pulses, separated in time by a variable period as short as one microsecond [92-97]. While reported "burst-mode" Nd:YAG systems differ in detail, they share certain basic characteristics. Specifically, reported systems typically utilize a low power (order 100 mW) master oscillator (typically Nd:YAG) which is "sliced" into a burst train using either a pair of electro-optic Pockel cells [92-95], or an acousto-optic deflector [96]. An exception is the system reported in [97] in which a repetitively Q-switched diode pumped Nd:YVO$_4$ laser is used as the master oscillator. The burst train is then amplified in a series of flashlamp-pumped Nd:YAG amplifiers. Typical reported burst sequences consist of between 8 – 40 pulses, with interpulse spacing as low as 1 μs, and individual pulse duration of between 6 and 25 ns.

Figure 33 shows the optical layout for the burst-mode Nd:YAG system being developed at Ohio State University, which is based on the system originally developed by Wu, et a. [92]. A single frequency, cw Nd:YAG ring laser serves as the primary oscillator, the output of which is pre-amplified in a standard double-pass flashlamp-pumped, pulsed Nd:YAG amplifier. While previous systems [92-95] utilized fixed, ~150–300 μs pulse duration power supplies to drive the lamps, we have recently incorporated a set of commercially available (Analog Modules – Series 8800 V) variable pulse duration flashlamp drivers so that the pre-amplified output consists of a single, temporally smooth 0.150 – 2.0 ms pulse, which is then formed into a "burst" train using a custom, dual electro-optic Pockels cell "slicer." Note that a similar, custom-designed variable 0.3 – 20 msec pulse width flashlamp supply will be incorporated into a system currently under development as a source for high-repetition-rate Thompson scattering [97]. The sliced pulse train is further amplified in a set of four additional flashlamp-pumped Nd:YAG amplifiers, with a stimulated Brillouin scattering (SBS) Phase Conjugate Mirror (PCM) located between amplifiers 3 and 4. The PCM, which acts as a non-linear intensity-dependent mirror, serves to eliminate a low-intensity "pedestal" superimposed on the high-intensity burst train, which results from the finite on/off contrast (~10^3–10^4) of the Pockel cell slicer [93]. Similarly, it also serves to reduce the exponential growth of amplified spontaneous emission (ASE) in the forward direction, by providing isolation between the first three and final two amplification stages [93].
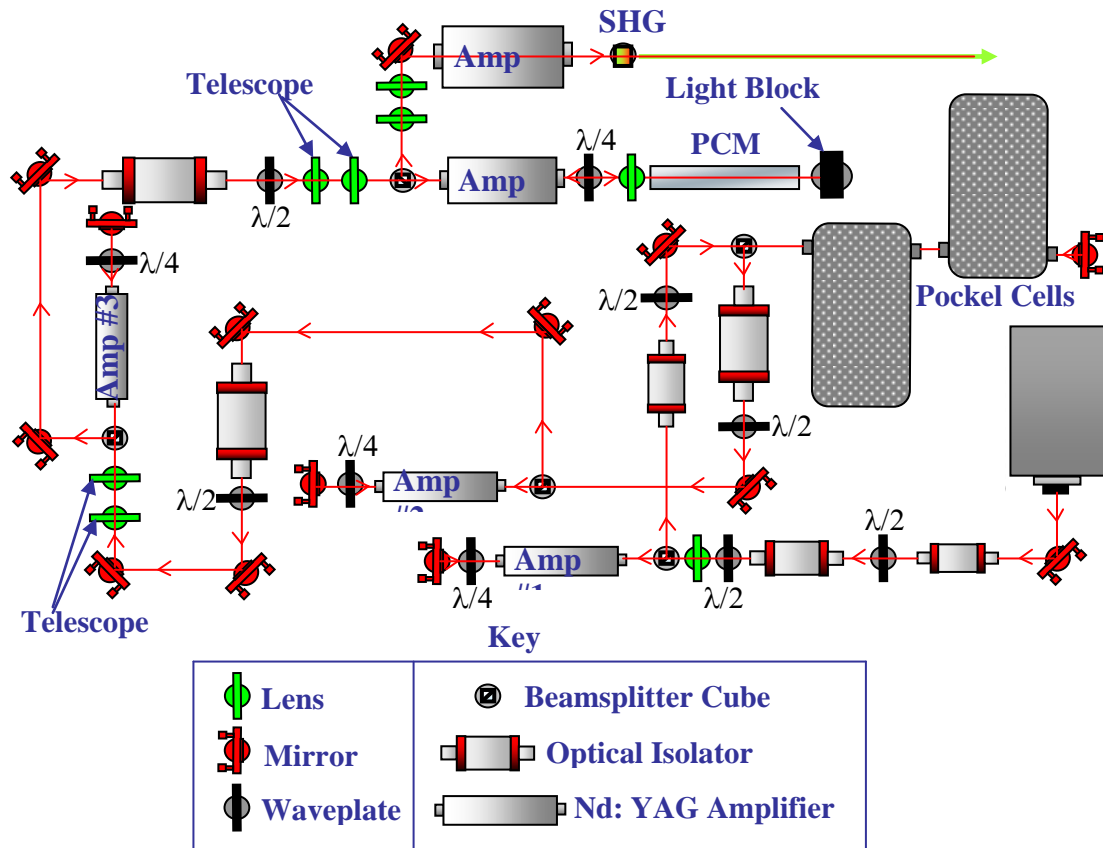
Figure 33
Schematic Diagram of OSU Pulse Burst Nd:YAG Laser.

As an example of the capabilities of the Nd:YAG pump laser, Fig. 34 shows four representative burst sequences for the fundamental output at 1064 nm [98]. The upper left trace shows a ten pulse burst with 10- μs interpulse spacing, with average energy per pulse of ~85 mJ. The upper right trace shows a burst of twenty pulses with 20-μs spacing and average individual pulse energy of ~230 mJ. At this repetition rate, similar to commercial "double-pulse" Nd:YAG systems, the time interval between the pulses is sufficient to allow partial refilling of the gain prior to the next pulse, resulting in higher and more uniform pulse energy. The lower left trace shows a sequence consisting of twenty pulses at 50-μs spacing. The average individual pulse energy is ~400 mJ/pulse, corresponding to a total extracted energy of 8 Joules. Finally the bottom right trace shows a 99 pulse burst at 10 microsecond spacing, with average individual pulse energy of approximately 27 mJ. While this is somewhat low, it is more than enough for a variety of scattering based diagnostics. For example, as will be discussed below, we have recently employed the Planar Doppler Velocimetry (PDV) method to perform quantitative velocity imaging at frame rates up to 250 kHz using pulse bursts of ~1-10 mJ/individual pulse (at 532 nm) [99]. Note that a relatively high input impedance (~10 kΩ) was used to capture the bursts in Fig. 34 on a standard digital oscilloscope. The true pulse durations are ~6 and 4 ns, for the 1064 nm and 226 nm wavelengths (lower right trace), respectively.
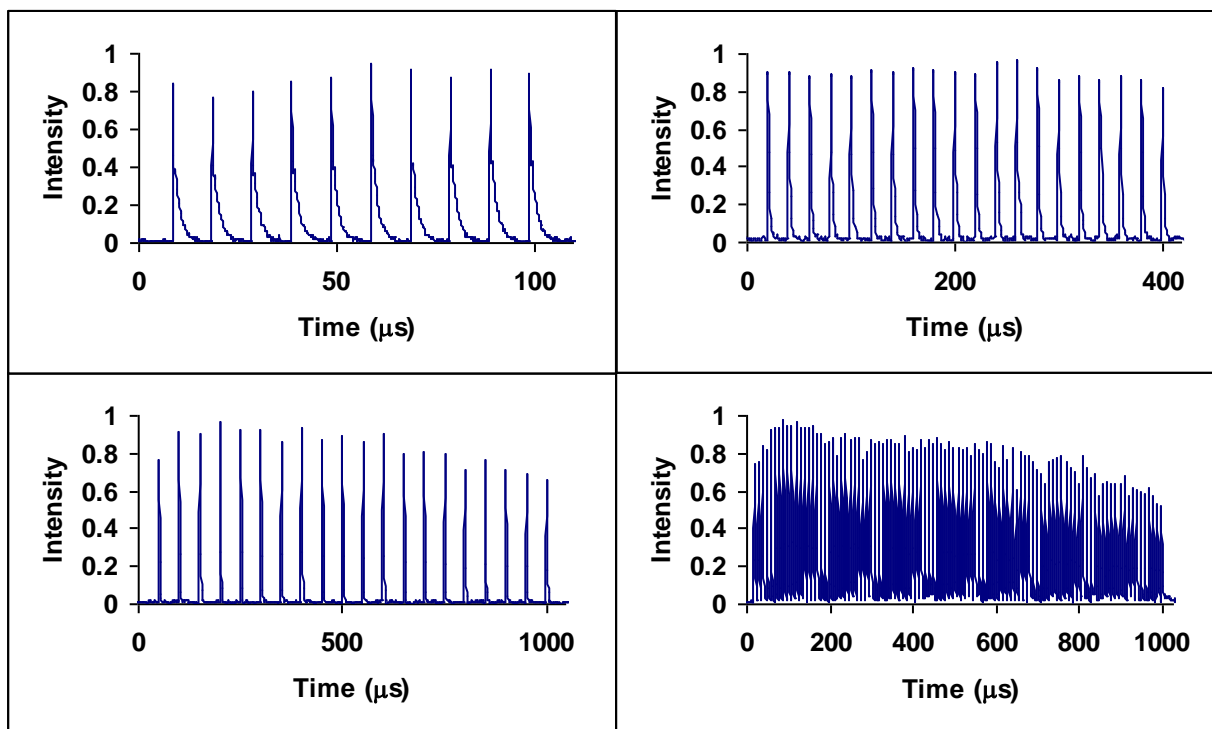
Figure 34

Representative burst sequences at 1064 nm using the system shown in Fig. 33. Upper left is 10 pulse sequence with 10 microsecond spacing and average individual pulse energy of 83 mJ. Upper right is 20 pulse sequence with 20 us spacing and 233 mJ/pulse. Lower left is 20 pulses with 50 us spacing. The average individual pulse energy is 420 mJ. Lower right is 99 pulse sequence with 10 microsecond spacing, the average individual pulse energy is 27 mJ.

The OSU burst mode laser, paired with a high frame rate imaging CCD camera [100], has been used for a variety of studies including: flow visualization [101] and quantitative velocimetry [102] measurements of convective velocity in supersonic (Mach 1.3 and 2) axisymmetric jets, aero optic wave front sensing [103], and impinging supersonic jet flow [104]. As one example, Fig. 35 summarizes the principle results of the axisymmetric Mach 2 turbulent jet convective velocity study. This work utilized Planar Doppler Velocimetry (PDV) which measures instantaneous velocity fields over a two-dimensional plane by resolving the scattered Doppler shift with a molecular iodine filter [29]. The convective velocity of large scale structures is obtained by applying a spatial cross correlation procedure to a series of individual images from a high speed (100 kHz) "movie", which is obtained with the burst mode imaging system [102]. The lower left graph in each of the two sets of graphs in Fig. 35 is a histogram of individual convective velocity values, each obtained from a single movie sequence (more than one hundred movies were obtained). The left graph is the result when ordinary flow visualization is used to define the fluid structures which are tracked. As can be seen, a bi-modal distribution results, with peaks that are both lower and higher than the convective velocity value of 205 m/sec predicted theoretically [105]. The right graph is the result when quantitative velocity is used to define the structures. It can be seen that defining structures in terms of their velocity, rather than simple intensity, results in a qualitatively different result, one which gives a single symmetric

distribution with mean value which agrees virtually perfectly with theory. More detail is given in [102].
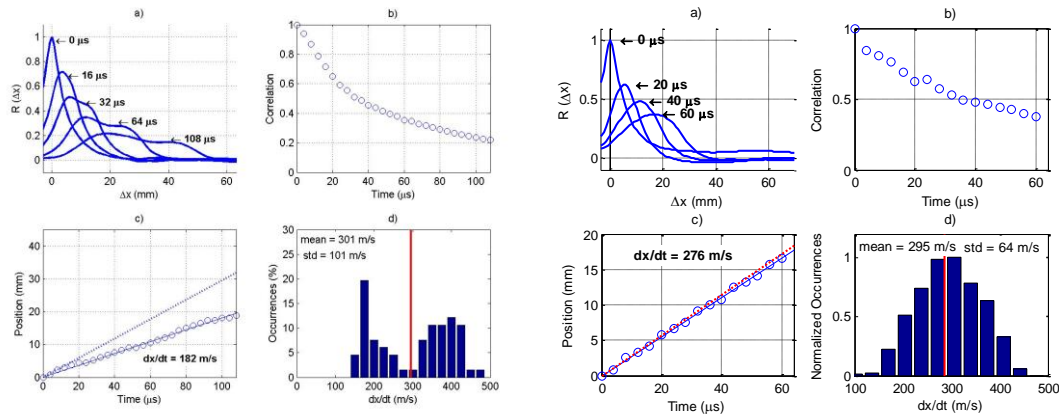

Figure 35

Comparison of convective velocity of large scale structures in Mach 2 turbulent axisymmetric jet when measured by flow visualization (left) and velocimetry (right), using OSU ultra high frame rate imaging system. From [102].

More recently we have enhanced the OSU ultra high frame rate imaging system by developing the capability to perform high (up to 500 kHz) Planar Laser Induced Fluorescence (PLIF) imaging [98, 106-108]. This is accomplished by utilizing a simple, home built, injection-seeded OPO system, pumped by the third harmonic output of the burst mode YAG system, as a source of tunable, narrow line width high repetition rate output. The output of the OPO can then be frequency doubled, and/or mixed with residual second (532 nm) or third harmonic (355) output from the YAG to produce tunable output in the ultra-violet. The system and its performance are described in detail in [106] and [107]. As an example, Fig. 36 shows a a typical 20 pulse - 10 μs spacing burst at 226 nm, which is used for NO PLIF imaging. For this example, the average individual single-pulse energy at 226 nm is ~0.5 mJ, which as will be shown, is sufficient to obtain NO PLIF images.
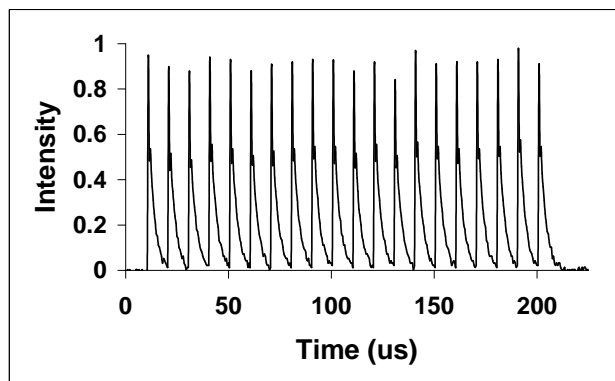

Figure 36

Typical 20 pulse burst sequence at 226 nm and 100 kHz burst frequency from OSU burst mode PLIF imaging system. Average individual pulse energy is ~0.5 mJ.

As a first example of ultra-high frame rate PLIF imaging, Fig. 37 shows a sequence of NO PLIF images in a laboratory scale Mach 3 wind tunnel, obtained using the well-known A $^2\Sigma$ (v'=0) $\leftarrow$ X $^2\Pi_{1/2}$ (v"=0) transition. The left side shows a typical sequence obtained at 250 kHz burst frequency, whereas the right is a sequence at 500 kHz. In both cases the field-of-view is ~9.5 (horizontal) x 7.1 (vertical) mm, centered 13 mm downstream from the location of a 1 mm diameter NO seeded sonic jet, which is located on the bottom wall of the tunnel. The Mach 3 flow is from left to right and the jet is injected from the bottom at a location approximately 5 mm upstream of the leading edge of the observation window. While this facility was not designed as a "jet in cross flow," the evolution and downstream progression of large scale structures, formed by the interaction between the jet and main flow, are clearly evident, particularly at the higher frame rate. Full details are given in [98].
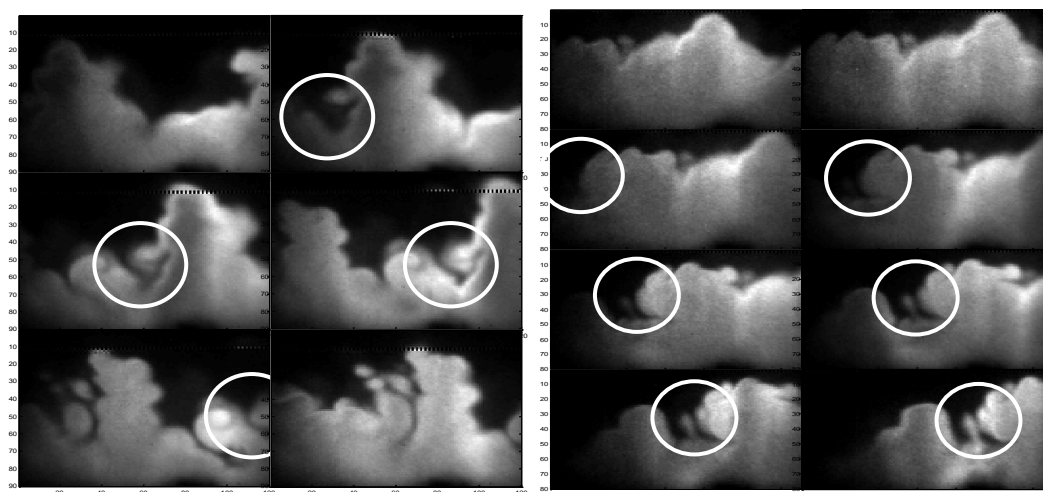

Figure 37

Sequence of NO PLIF images in laboratory scale Mach 3 flow taken with OSU burst mode PLIF system at 250 kHz (left) and 500 kHz (right) frame rate.

As a second example, OH PLIF imaging has also recently been demonstrated using a diode laser–seeded OPO cavity which is essentially identical to that used for NO, but pumped at 532 nm [108]. Starting with ~100 mJ/pulse at 532 nm, signal output at 763 nm is sum-frequency mixed with the residual 532-nm pump, resulting in ~1 mJ per pulse at 313.526 nm. Fig. 38 shows a partial series of images (20 total were obtained) from a 1-mm-diameter H_2/air diffusion flame obtained at a burst frequency of 25 kHz (up to 50 kHz has been demonstrated). The temporal evolution of flame structures can be tracked in the image sequence, with turbulent eddies along the interface influencing the mixing process and local combustion chemistry. For example, the evolution of a flame layer is marked with a white circle in Fig. 38 as it is pinched off from the main reaction zone and subsequently extinguished. These results illustrate the ability of the current system to track turbulent flame phenomena through the relevant times scales of fluid-flame interaction. Full detail is given in [108].
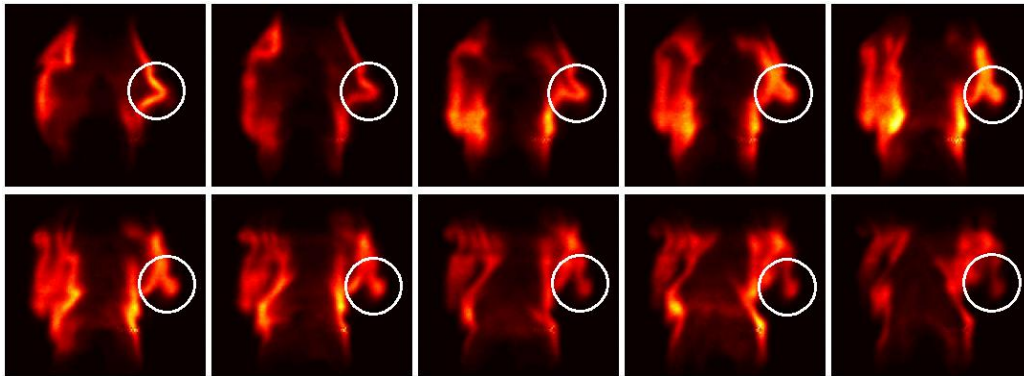
Figure 38
Ten, of a total of twenty, OH-PLIF images obtained from atmospheric-pressure turbulent H_2-air diffusion flame at 25-kHz repetition rate. From Ref [108].

We end this section by noting some very recent progress towards the development of three-dimensional imaging of high speed flows [109]. Using a burst mode Nd:YAG system similar to that described in [96], in combination with a high speed mirror, Thurow has obtained a "stack" of 68 planar images from a turbulent jet (Reynolds number 7600, exit velocity ~3.2 m-sec^{-1}), at a frame rate of 500 kHz. The use of a reconstruction technique, described in [109], results in high quality, three dimensional images of the highly turbulent flow structure downstream of the jet exit, an example of which is shown in Fig. 39.
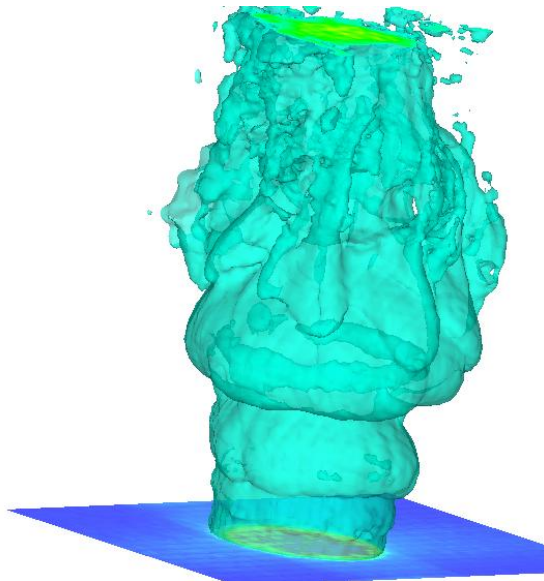

Figure 39
Experimental three dimensional image of turbulent jet obtained using high speed imaging system under development at Auburn University. From [109].

5 Conclusions and Acknowledgements

This lecture has presented a representative survey of a subset of recent applications of optical diagnostic methods to studies of non-equilibrium flows and plasmas, with emphasis on measurements in air, and oxygen containing environments. While the survey is by no means complete, it is hoped that it will provide researchers in this field with an overview of the power of modern optical methods, and a sense of how they can be employed as tools for detailed study and characterization of non-equilibrium environments.

REFERENCES

1. Eckbreth, A.C., *"Laser Diagnostics for Combustion Temperature and Species",* 2nd Ed., Gordon and Breach Publishers, Amsterdam, 1996.

2. M. A. Linne, *"Spectroscopic Measurement – An Introduction to the Fundamentals,"* Academic Press, Amsterdam, 2002.

3. K. Kohse-Hoinghaus and J. B. Jeffries, *"Applied Combustion Diagnostics,"* Taylor and Francis, New York, 2002.

4. W. Demtroder, *"Laser Spectroscopy – Basic Concepts and Instrumentation,"* Springer, Berlin, 2nd Edition, 1996.

5. G. Laufer, *"Introduction to Optics and Lasers in Engineering,"* Cambridge University Press, Cambridge, 1996.

6. W. Lempert in *Non-Equilibrium Air Plasmas at Atmospheric Pressure*, edited by Becker, K., Kogelschatz, U., Schoenbach, K.H., and Barker, R., IOP Publishing, Bristol, UK, 2005, Chapter 8, "Diagnostics."

7. Dicke, R.H., *"Physical Reviews",* Vol. 89, p. 472 (1953).

8. Bonamy, L., Bonamy, J., Robert, D., Lavorel, B., Saint-Loup, R., Chaux, J., Santos, J., and Berger, H., *Journal of Chemical Physics*, Vol. 89, p. 5568 (1988).

9. Rosasco, G.J., Lempert, W., Hurst, W.S., and Fein, A., in "Spectral Line Shapes, Vol 2, Walter de Gruyter & Co., Berlin, p. 635 (1983).

10. Galatry, L., *Physical Reviews*, Vol 122, p. 1281 (1961).

11. Hall, R.J., Verdieck, J.F., and Eckbreth, A.C., Optics Communications, Vol. 35, p. 69 (1979).

12. D.A. McQuarrie and J.D Simon, *"Physical Chemistry – A Molecular Approach,"* University Science Books, Sausilito CA, 1997.

13. M.G. Allen, E.R. Furlong, and R.K. Hanson, "Tunable Diode Laser Sensing and Combustion Control," in *"Applied Combustion Diagnostics,"* edited by K. Kohse-Hoinghaus and J. B. Jeffries, Taylor and Francis, New York, 2002.

14. B.K. McMillan, J.L. Palmer, and R.K. Hanson, Appl. Opt. 32, 7532- 7545 (1993).

15. W. Lee and W. R. Lempert, "Spectrally Filtered Raman/Thomson Scattering using a Rubidium Vapor Filter," AIAA Journal, Vol 40, No. 12, 2002, pp. 2504 –2510.

16. A.B. Harvey, *Chemical Applications of Nonlinear Raman Spectroscopy,"* Academic Press, New York, 1981.

17. R.A. Parker, T. Wakeman, M. MacLean, and M. Holden, AIAA-2006-926, 44th AIAA Aerospace Sciences Meeting, Reno, NV, 9-12 January, 2002.

18. M. Holden and R.A. Parker, "Lens Hypervelocity Tunnels and Application to Vehicle Testing at Duplicated Flight Conditions," Chapter 4, Advanced Hypersonic Test Facilities, Editors F. Lu and D. Marren, Vol 198, 2002.

19. G. Herzberg, *"Molecular Spectra and Molecular Structure – Vol I Spectra of Diatomic Molecules,"* Krieger Publishing Company, Malibar, FL, reprint edition (1989).

20. L.S. Rothman, A. Barbe, D.C. Benner, L.R. Brown, C. Camy-Peyret, M.R. Carleer, K.V. Chance, C. Clerbaus, V. Dana, V.M. Devi, A. Fayt, J.M. Flaud, R.R. Gamache, A. Goldman, D. Jacquemart, K.W. Jucks, W.J. Lafferty, J.Y. Mandin, S.T. Massie, V. Nemtchinov, D. Newnham, A. Perring, C.P. Rinsland, J. Schroeder, K. Smith, M.A.H. Smith, K. Tang, R.A Toth, J. Vander Auwerea, P. Varanasi, K. Yoshing, "The HITRAN molecular spectroscopic database: editor of 2000 including updates through 2001," JQSRT 82, p.5 (2003).

21. K.Frederickson, W. Lee, P. Palm, I.V. Adamovich, J. W. Rich, and W.R. Lempert, "Mitigation of electron attachment to oxygen in high pressure air plasmas by vibrational excitation," J. Applied Physics, vol. 101, p. 093302, 2007.

22. Long, D.A., *The Raman Effect*, John Wiley & Sons, London, 2002.

23. Weber, A., *"Raman Spectroscopy of Gases and Liquids,"* Springer-Verlog, Berlin, 1979.

24. W. Lee and W. Lempert, "Enhancement of spectral purity of injection-seeded titanium:sapphire laser by cavity locking and stimulated Brillouin scattering, " Applied Optics, **42,** pp. 4320-4326, 2003**.**

25. Rasetti, F., *Nuovo Cimento*, Vol. 7, 1930, p. 261.

26. Pelletier, M.J., *Applied Spectroscopy*, Vol. 46, No. 3, 1992, pp. 395-400.

27. Indralingan, R., Simeonsson, J.B., Petrucci, G.A., Smith, B.W., and Winefordner, J.D.W., *Analytical Chemistry*, Vol 64, 1991, pp. 964-967.

28. Clops, R., Fink, M., Varghese, P.L., and Young, D., *Applied Spectroscopy*, Vol 54, No. 9, 2000, pp. 1391 – 1398.

29. *Measurement Science and Technology*, Vol. 12, No. 4, 2001.

30. Shimizu, H., Lee, S.A., and She, C.Y., *Applied Optics*, Vol. 22, No. 9, 1983, pp. 1373 – 1381.

31. Bakker, L.P., and Kroesen, G.M., Journal of Applied Physics, Vol. 88, p. 3899 (2000).

32. Miles, R.B., Yalin, A.P., Tang, Zhen, Zaidi, S.H., Forkey, J.N., *Measurement Science and Technology*, Vol. 12, No. 4, 2001, pp. 442-451.

33. W. Lee, K. Frederickson, P. Palm, I. Adamovich, J.W. Rich, and W. Lempert, "Mitigation of Oxygen Attachment in High Pressure Plasmas by Vibrational Excitation, AIAA-2004-2257, 35th AIAA Plasmadynamics and Laser Meeting, Portland, OR, 28 Jun – 01 July, 2004.

34. C. E. Treanor, J. W. Rich and R. G. Rehm, Journal of Chemical Physics, vol. 48, 1798 – 1807 (1968).

35. J. H. Grinstead and P.F. Barker, Phys. Rev. Lett 85, p. 1222 (2000).

36. X. Pan, P.F. Barker, A. Meschavnov, J.H. Grinstead, and M.N. Shneider, and R.B. Miles, Opt. Lett. 27, p. 161 (2002).

37. Chiroux de Gavelle de Roany, A, Filament, C., Rich, J.W., Subramaniam, V.V., and Warren, W.R., AIAA Journal, Vol 31, p. 119, 1993.

38. Lee, W., Adamovich, I. V., and Lempert, W. R., *Journal of Chemical Physics*, Vol. 114, No., 3. 2001, pp. 1178-1186.

39. Y. P. Raizer, "Gas Discharge Physics", Springer-Verlag, Berlin, 1991.

40. Gresillon, D., Gemaux, G., Cabrit, B., and Bonnet, J.P., *European Journal of Mechanics B*, Vol. 9, p. 415 (1990).

41. Ornstein, L.S., and Zernike, F., *Phys. Z*, Vol 27, p. 761 (1926).

42. B.J. Berne and R. Pecora, *"Dynamic Light Scattering,"* John Wiley and Sons, New York, 1976.

43. D. Messina, B. Attal-Tretout, and F. Grisch, Proceedings of the Combustion Institute Vol 3, p. 825 (2007).

44. S. M. Starikovskaia, N.B. Anikin, S.V. Pancheshnyi, and A. Yu Starikovskii, "Proceedings of the SPIE, vol 4460, p. 63 (2002).

45. M.S. Smith and J.J. Coblish, AIAA-2004-2399, 24th AIAA Aerodynamic Measurement Technology and Ground Testing Conference, Portland, OR, 28 June – 1 July 2004.

46. W.C. Ragsdale and C.F. Boyd, Hypervelocity Wind Tunnel 9 Facility Handbook," Technical Report NAVSWC TR 91-616, Naval Surface Warfare Center, Silver Spring, MD, July 1993.

47. G.V. Candler, AIAA-2002-0581, AIAA 40th Aerospace Sciences Meeting, Reno, NV, January, 2002.

48. M.S. Smith, AIAA-2006-2814, 25th AIAA Aerodynamic Measurement Technology and Ground Testing Conference, San Francisco, CA, 5-8 June, 2004.

49. D. Studer and P. Vervisch, J. Appl. Phys. Vol 102, p. 033303 (2007).

50. M. Uddi, N. Jiang, I. V. Adamovich, and W. R. Lempert, AIAA-2008-3884, 39 Plasmadynamics and Lasers Conference, 23-26 June 2008, Seattle, WA.

51. S. De Benedictis and G. Dilecce, J. Chem. Phys. Vol 107, p. 6219 (1997).

52. Gordiets B F, Ferreira C M, Guerra V L, Loureiro J M A H, Nahorny J, Pagnon D, Touzeau M, Vialle M, IEEE Trans. Plasma Sci., 23, 1995, p 750.

53. G Dilecce and S De Benedictis, "Experimental studies on elementary kinetics in N_2–O_2 pulsed discharges", Plasma Sources Sci. Technol. 8 (1999) 266–278.

54. Guerra V, Loureiro J, J. Phys. D : J. Appl. Phys., 28, 1995, p 1903.

55. G. Dilecce, P.A. Ambrico, and S. DeBenedictis, Plasma Sources Sci. Technol., vol 14, p. 561 (2005).

56. G. Dilecce, P.A. Ambrico, and S. DeBenedictis, Czech J. Phys, vol 56, p. B690 (2006).

57. C. Foissac, A. Campargue, A. Kachanov, P.Supiot, G. Weirauch, and N. Sadeghi, J. Phys. D:Appl. Phys., vol 33, p. 2434 (2000).

58. G.D. Stancu, M. Janda, F. Kaddouri, D. Pai, D.A. Lacoste, J.C. Rolon, and C.O. Laux, AIAA-2008-3882, 38th AIAA Plasmadynamics and Lasers Conference, 23-26 Jun 2008, Seattle, WA.

59. W.E. McDermott, N.R. Pchelkin, D.L> Benard, and R.R. Bousek, Appl. Phys. Lett. 32, p.469 (1978).

60. D.L. Carroll, J.T. Verdeyen, D.M. King, J.W. Zimmerman, J.K. Laystrom, B.S. Woodard, G.F. Benavides, K. Kittell, D.S. Stafford, M.J. Kushner, and W.C. Solomon, Appl. Phys. Lett., vol. 86, 2005, pp. 111104-111104-3.

61. A. Hicks, Yu.G. Utkin, W.R. Lempert, J.W. Rich, and I.V. Adamovich, Applied Physics Letters, vol. 89, 2006, pp. 241131-241131-3.

62. A. Hicks, J. Bruzzese, W.R. Lempert, J.W. Rich, and I.V. Adamovich, Applied Physics Letters, vol. 91, p. 071116, 2007.

63. S. Williams, M. Gupta, T. Owano, D.S. Baer, A. O'Keefe, D.R. Yarkony, and S. Matsika, Optics Lett. 29, 1066 (2004).

64. M.Gupta, T. Owano, D.S. Baer, A. O'Keefe, S. Williams, Chem. Phys. Lett. 400, 42 (2004).

65. A.P. Yalin, C.O. Laux, C.H. Kruger, and R.N. Zare, Plasma Sources Sci. and Technol. 11, p. 248 (2002).

66. A.P. Yalin, C.O. Laux, C.H. Kruger, and R.N. Zare, Appl. Phys. Lett 81, p. 1408 (2002).

67. S. Spuler, and M. Linne, Appl. Opt 41, p. 2858 (2002).

68. Noguchi, Y., Matsuoka, A., Bowden, M.D., Uchino, K., and Muraoka, K., Japanese Journal of Applied Physics, Vol. 40, No. 1, 2001, pp. 326-329.

69. D.L. Crintea, D. Luggenholscher, V.A. Kadetov, Ch Isenber, and U. Czarnetzki, J. Phys D: Appl. Phys. 41, 082003, 2008.

70. Bakker, L.P., J.M. Freriks, F.J. deGroog, and G.M.W. Kroesen, *Review of Scientific Instruments*, Vol. 71, No.5, 2000, pp. 2007-2014.

71. Miles, R.B., Yalin, A.P., Tang, Zhen, Zaidi, S.H., Forkey, J.N., *Measurement Science and Technology*, Vol. 12, No. 4, 2001, pp. 442-451.

72. Penney, C. M., St. Peters, R. L., and Lapp, M., *Journal of the Optical Society of America*, Vol. 64, No. 5, 1974, pp. 712-716.

73. Kim, W., Do, H., Mungal, M.G, and Cappelli, M, IEEE Trans on Plasma Science 34, p. 2545 (2006).

74. Kim, W., Do, H., Mungal, M.G, and Cappelli, M, Proceedings of Combustion Institute 31, p. 3319 (2007).

75. Pilla G, D. Galley, D. Lacoste, F. Lacas, D. Veynante, and C. Laux, AIAA Paper 2006-3243, 37th AIAA Plasmadynamics and Lasers Conference, San Francisco, CA, 2006.

76. S.A. Bozhenkov, S.M. Starikovskaya, and A.Yu. Starikovskii, Combustion and Flame, vol. 133, 2003, pp. 133-146

77. A. Yu. Starikovskii, Proceedings of the Combustion Institute 30 (2005) 2405-2417.

78. A. Bao, Yu.G. Utkin, S. Keshav, G. Lou, and I.V. Adamovich, "Ignition of Ethylene-Air and Methane-Air Flows by Low-Temperature Repetitively Pulsed Nanosecond Discharge Plasma", accepted for publication by IEEE Transactions on Plasma Science, 2007

79. G. Lou, A. Bao, M. Nishihara, S. Keshav, Y.G. Utkin, J.W. Rich, W.R. Lempert, and I.V. Adamovich, Proceedings of the Combustion Institute, vol. 31, Issue 2, January 2007, pp. 3327-3334.

80. M. Uddi, N. Jiang, E. Mintusov, I. V. Adamovich, and W. R. Lempert, PROCI-D-07-00123R1, Proceedings of the Combustion Institute, Accepted for Publication, May, 2008 (2008 Combustion Symposium, Montreal CA).

81. E. Mintusov, A. Serdyuchenko, I. Choi, W.R. Lempert, and I.V. Adamovich, "Mechanism of Plasma Assisted Oxidation and Ignition of Ethylene-Air Flows by a Repetitively Pulsed Nanosecond Discharge," PROCI-D-07-, Proceedings of the Combustion Institute, Accepted for Publication, May, 2008 (2008 Combustion Symposium, Montreal CA).

82. Bamford J D, Jusinski L E, Bischel W K, 1986, Vol 34, No 1, Physical Review A, pp 185- 198

83. Bischel W K, Perry B E, Crosley D R, 1982, Vol 21, No 8, Applied Optics, pp 1419-1429

84. Tserepi A D, Miller T A, Journal of Applied Physics, pp 505-511.

85. Niemi K., Gathen V. S. and H F Dobele H. F., Plasma Sources Sci. Technol. 14 (2005) 375–386

86. Fletcher, D. "Arcjet flow properties determined from laser-induced fluorescence of atomic nitrogen." Applied Optics, v. 38, pp. 1850-1858, 1999.

87. Grinstead, J.H., Driver, D.M., and Raiche, G.A., 2002, AIAA-2002-0398, 40th AIAA Aerospace Sciences Mtg, Reno, NV

88. M. Uddi, N. Jiang, E. Mintusov, I.V. Adamovich, and W.R. Lempert, AIAA-2008-1110, 46th AIAA Aerospace Sciences Meeting, Jan, 2008, Reno, NV.

89. http://www.me.berkeley.edu/gri_mech/version30/text30.html, GRI-Mech 3.0.

90. H. Wang, X. You, A.V. Joshi, S.G. Davis, A. Laskin, F. Egolfopoulos, and C.K. Law, USC Mech Version II. http://ignis.usc.edu/USC_Mech_II.htm, May 2007.

91. E. Mintusov, A. Serdyuchenko, I. Choi, W.R. Lempert, and I.V. Adamovich, AIAA Paper 2008-1106, 46th Aerospace Sciences Meeting and Exhibit, 7-10 January 2008, Reno, NV.

92. P. Wu, W. R. Lempert, and R.B. Miles, AIAA J. **38**, 672-679 (2000).

93. B. Thurow, N. Jiang, M. Samimy, and W. Lempert, Appl. Opt. **43**, 5064-5073 (2004).

94. M. Wernet and A.B. Opalskii, AIAA-2004-2184, 24th Aerodynamic Measurement Technology & Ground Testing Conference, June 28-July 1, 2004, Portland, OR.

95. Alan L. Kastengren, J. Craig Dutton, and Gregory S. Elliott, Phys. Fluids 19, 015103 (2007).

96.   B. Thurow and A. Satija, AIAA-2006-1384, 44th AIAA Aerospace Sciences Mtg, Reno, NV, Jan, 2004.

97.   D. J. Den Hartog, N. Jiang, and W. R. Lempert, accepted for publication in Rev. Sci. Instrum.

98.   N. Jiang, M. Webster, and W.R. Lempert, Accepted for publication in Applied Optics, September, 2008.

99.   B. Thurow, N. Jiang, W. Lempert, and M. Samimy, AIAA J., **43**, 500-511 (2005).

100.   Princeton Scientific Instruments, Inc. www.prinsci.com

101. B. Thurow, M. Samimy, and W. Lempert, Physics of Fluids, **15**, pp. 1755-1765, 2003.

102. B.S. Thurow, N. Jiang, J-H Kim, W. Lempert, and M Samimy, Physics of Fluids, vol 20, pp**.** 066101**-1 -** 066101-15 , 2008.

103. B. Thurow, M. Samimy, W. Lempert, S.R. Harris, J. Widiker, and B. Duncan, AIAA-2003-0684, 41st AIAA Aerospace Sciences Meeting, Reno, NV, January 6-9, 2003.

104. B. Thurow, M. Samimy and W. Lempert, AIAA-2002-2865, 32nd AIAA Fluid Dynamics Conference, St. Louis, MS, June 24-26, 2002.

105.   D. Papamoschou and A. Roshko J. Fluid Mech. **197**, 453 (1988).

106. N. Jiang, W.R. Lempert, G.L. Switzer, T.R. Meyer, and J.R. Gord, Applied Optics, Vol 47, pp. 64-71, 2008

107. N. Jiang and W. R. Lempert, "Ultra-high frame rate Nitric Oxide Planar Laser Induced Fluorescence imaging," Optics Letters, **33**, October, 2008.

108. J. D. Miller, M. Slipchenko, T. R. Meyer, N. Jiang, W. R. Lempert , J. R. Gord , "Ultrahigh-frame-rate OH fluorescence imaging in turbulent flames using a burst-mode optical parametric oscillator," submitted to Optics Letters, July, 2008.

109. B. Thurow, AIAA-2008-4269, 26th AIAA Aerodynamic Measurement Technology and Ground Testing Conference, Seattle, WA, 23-26 June, 2008.